LBL-33608
UC-419

Lawrence Berkeley Laboratory

UNIVERSITY OF CALIFORNIA

Accelerator & Fusion Research Division

Space-charge Dominated Beam Transport in Magnetic Quadrupoles with Large Aperture Ratios

W.F. Fawley

August 1993

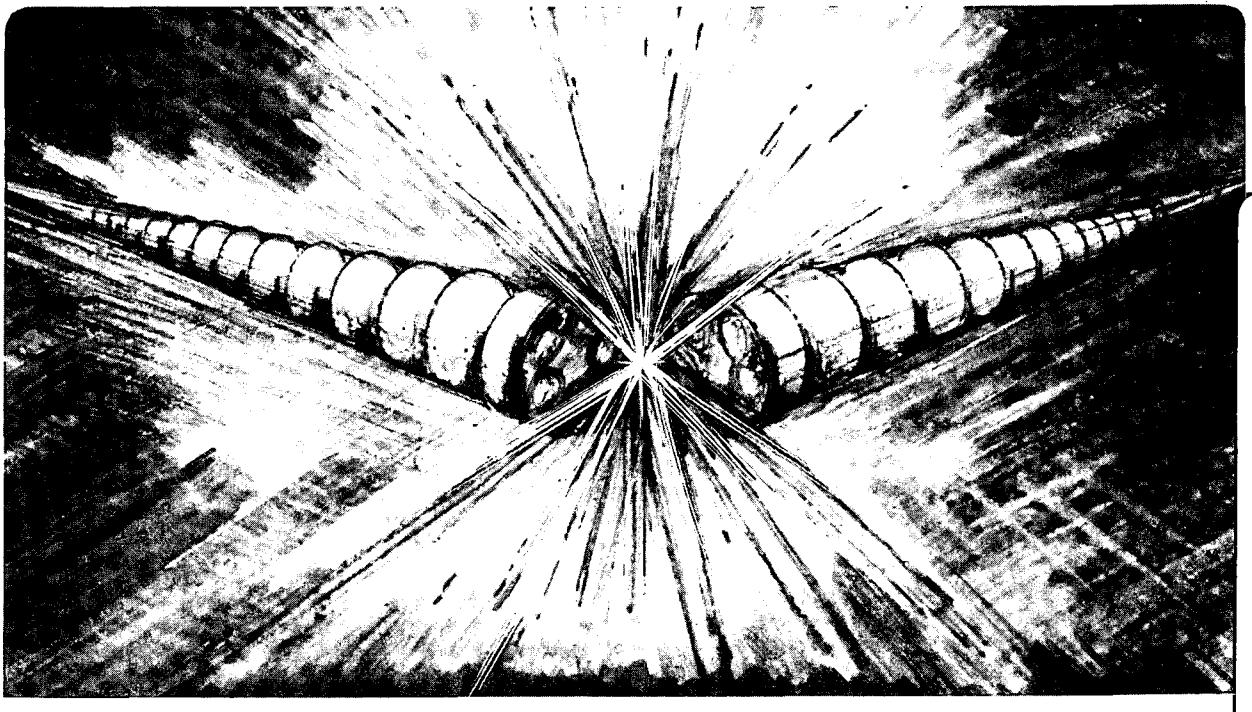

REFERENCE COPY
Does Not
Circulate
Bldg. 50 Library.
LBL-33608
Copy 1

Prepared for the U.S. Department of Energy under Contract Number DE-AC03-76SF00098

DISCLAIMER

This document was prepared as an account of work sponsored by the United States Government. Neither the United States Government nor any agency thereof, nor The Regents of the University of California, nor any of their employees, makes any warranty, express or implied, or assumes any legal liability or responsibility for the accuracy, completeness, or usefulness of any information, apparatus, product, or process disclosed, or represents that its use would not infringe privately owned rights. Reference herein to any specific commercial product, process, or service by its trade name, trademark, manufacturer, or otherwise, does not necessarily constitute or imply its endorsement, recommendation, or favoring by the United States Government or any agency thereof, or The Regents of the University of California. The views and opinions of authors expressed herein do not necessarily state or reflect those of the United States Government or any agency thereof or The Regents of the University of California and shall not be used for advertising or product endorsement purposes.

This report has been reproduced directly
from the best available copy.

Available to DOE and DOE Contractors
from the Office of Scientific and Technical Information
P.O. Box 62, Oak Ridge, TN 37831
Prices available from (615) 576-8401, FTS 626-8401

Available to the public from the
National Technical Information Service
U.S. Department of Commerce
5285 Port Royal Road, Springfield, VA 22161

Lawrence Berkeley Laboratory is an equal opportunity employer.

DISCLAIMER

This document was prepared as an account of work sponsored by the United States Government. While this document is believed to contain correct information, neither the United States Government nor any agency thereof, nor the Regents of the University of California, nor any of their employees, makes any warranty, express or implied, or assumes any legal responsibility for the accuracy, completeness, or usefulness of any information, apparatus, product, or process disclosed, or represents that its use would not infringe privately owned rights. Reference herein to any specific commercial product, process, or service by its trade name, trademark, manufacturer, or otherwise, does not necessarily constitute or imply its endorsement, recommendation, or favoring by the United States Government or any agency thereof, or the Regents of the University of California. The views and opinions of authors expressed herein do not necessarily state or reflect those of the United States Government or any agency thereof or the Regents of the University of California.

LBL-33608
UC-419
HIFAN# 614

Space-charge Dominated Beam Transport in Magnetic Quadrupoles with Large Aperture Ratios

William M. Fawley
Accelerator & Fusion Research Division
Lawrence Berkeley Laboratory
University of California
Berkeley, California 94720

*This work was supported by the Office of Energy Research, Office of Fusion Energy, U.S. Department of Energy under Contract No. DE-AC03-76SF00098.

recycled paper

Space-charge Dominated Beam Transport in Magnetic Quadrupoles with Large Aperture Ratios

William M. Fawley

Abstract

This memo summarizes the results of calculations of the usable aperture ratio for short period, magnetic quadrupoles for both ILSE magnet designs and the more general, heavy-ion fusion (HIF) "driver" case. From both analytic decomposition of the magnetic field in a periodic lattice and particle code simulations of beam transport, we find that fringe field nonlinearities and associated emittance growth become quite large when the beam radius a_b exceeds one-quarter or so of the half-lattice period L. For ILSE, there are a number of magnet designs which can transport the specified line charge without any significant difficulties, primarily because the ratio a_b/L is of order 0.1 or less. For larger sized beams such as one might employ in the low energy part of a driver, there are problems with properly matching the beam to the transport lattice in both the macroscopic and microscopic sense as a_b/L exceeds 0.2. For even larger aperture ratios, particle loss can occur, with the threshold in beam radius roughly scaling inversely with σ_o, the single particle phase advance per lattice period.

I. Introduction

An important issue in the design of heavy ion fusion drivers is the dynamic aperture of short period quadrupoles. In standard driver designs, these immediately follow the transition from electrostatic to magnetostatic focusing. This memo outlines the results of recent calculations concerned with the dynamic aperture for both ILSE magnet designs and the limiting case of large aperture ratio† quads as might be considered for a driver. This memo also delineates, for "archival" purposes, the set of analytical and computational tools used in this study. Much of this work has been done in close consultation with and relies upon previous work by L.J. Laslett, V. Brady, S. Caspi, C. Celata, A. Faltens, and I. Haber. I acknowledge with pleasure their assistance, and the time spent by the last three persons on critical readings of this manuscript.

The interest in short period quads evolved from the fact that the maximum transportable current for a space-charge dominated beam scales as the usable beam aperture, a_b, squared:

$$I_{max} \approx \left(\frac{a_b}{2L}\right)^2 I_o \frac{A\gamma^3\beta^3}{2Q}\sigma_o^2 \tag{1}$$

Here I_o is the proton "Alfven current", 31.07 MA, A and Q are the atomic mass and charge state respectively of the ion species, γ and β have the normal Lorentz definitions, L is the half-lattice period, and σ_o is the betatron phase advance per full lattice period in the absence of space charge. Since a large I_{max} permits more efficient use of the accelerating core cross-section and thus less cost, there is great premium in making the beam aperture as large as possible.

The usable aperture a_b may be defined as that above which the beam suffers unacceptable emittance growth and/or particle loss over the transport distance of interest. Although we have not specified any hard or fast values for ILSE, a reasonable limit on emittance growth might be 50%, while particle loss should be kept quite small (< 1%). Similar criteria apply to most linear HIF driver designs. For a recirculator driver with dozens of turns per ring and multiple rings, the average emittance growth per turn probably must be limited to a half-percent or less.

Furthermore, physically a_b must remain somewhat smaller than a_{wire}, the radius of the magnet wire windings. As the aperture ratio (a_{wire}/L) of a magnetic quad is increased, a number of phenomena degrade the field quality.

† To dispel possible confusion, in correct English usage, the aperture ratio is the inverse of the "aspect ratio" (L/a).

First, the $\cos 2\theta$ fringe field components near the ends of the magnet begin to be increasingly important relative to the wanted z–independent components that dominate in the center of the magnet. L.J. Laslett [1] showed how the quadrupole $\hat{z}$ component of the vector potential can be expanded as

$$A_z \approx \left[A_2(z)\, r^2 - \frac{1}{12} A_2''(z)\, r^4 + \frac{1}{384} A_2^{iv}(z)\, r^6 \right] \cos 2\theta \qquad (2)$$

where the primes refer to z-derivatives. The so-called 'pseudo-octupole' term [2](*i.e.* the second term in the brackets whose radial r^4 dependence is that of an octupole but whose azimuthal dependence is quadrupolar) will be present to some extent in all realizable 3-D quadrupole magnet lattices. Although the average (z-integrated at constant radius) pseudo-octupole field must vanish both for an isolated quad and over a full lattice period in a FODO array, such is not necessarily the case over a single half-period, especially when the focusing and defocusing quads lie close enough ($\leq 2a_{wire}$) in z that their fringe fields interfere. Moreover, in typical HIF situations where σ_0 is relatively large, A. Faltens has suggested that convolution of the AG flutter motion with the pseudo-octupole fields can lead to net forces on the individual particles, even when the longitudinal average of $A_2''(z)$ (at constant radius) is zero over a half-lattice period. These forces are anharmonic and may lead to emittance growth.

In addition to pseudo-octupole terms, there will usually be dodecapole or higher order azimuthal components. These arise from the limitation that azimuthally discrete windings cannot produce a locally (in z) perfect $\cos 2\theta$ magnetic field dependence. Instead, the field will have azimuthal overtones of $\cos(4l+2)\theta$ for $l = 1, 2, \ldots$. The lowest overtone, the dodecapole, generally dominates until one gets very close radially to an individual winding. The usual means [1,3-4] taken to minimize these unwanted overtones is to force their z-integrated contribution at constant radius to zero for a given individual quad, much as occurs naturally for the pseudo-octupole term of each end of an isolated quad.

The remainder of this memo is organized in the following fashion. We discuss in §II our design process for short period quadrupoles. We have looked at four types of magnets of this type:

1) The "Laslett-Brady-Celata-Faltens" configuration [1] in which individual coil turns are rectangles in the developed view.

2) "Laslett-Caspi-Helm" configurations [4] in which turns in the developed view follow a specified algebraic relationship to eliminate the z-integrated overtone fields.

3) A "nested ellipse" configuration, a variant of the above, which uses straight sections terminated by elliptical curved ends to both eliminate z-integrated overtone fields and to maximize the radius of curvature.

4) A "Fourier-Bessel" configuration proposed by Laslett, where the current windings are positioned in an "infinite" periodic lattice in z such that the azimuthal field dependence follows a $\cos 2\theta$ dependence *exactly*, the radial dependence is a modified Bessel function, and the longitudinal dependence is a superposition of one or more discrete Fourier harmonics of the fundamental periodicity $2L$.

The transport properties of these designs for ILSE-like parameters are then reported in §III. For this study we used the HIFI particle code, a fast running particle code that uses 3-D external magnetic fields and, in its present version, expands the beam space charge fields as a reduced set of azimuthal multipoles. We then look at "absolute" aperture limits in §IV where we study particle loss and emittance growth as a function of σ_0 and (a_b/L). This is followed by a short concluding section, §V, which itself is followed by appendices discussing field algorithms and the HIFI simulation code.

II. Quadrupole Magnet Design Process

The ideal short quadrupole magnet would

a) maximize quadrupole field strengths for a given current excitation

b) have an effective length† comparable to that of the maximum longitudinal extent of the windings

c) have no azimuthal overtone fields (*e.g.* dodecapole fields)

d) have all fringe fields longitudinally confined to a quite narrow region

e) be amenable to construction with discrete superconducting cable (*i.e.* bend radii of curvature ≥ 10 mm, no iron in the immediate vicinity of the cables, magnetic field strengths at the wires well below the quench point)

Our present design process has concentrated on point (c) with attention being paid to point (e) in some of the later designs. With the exception of the idealized "Fourier-Bessel" design, all other designs have compromised on point

† We define the effective length ηL in a periodic lattice as $\int_0^L A_2(z)\, dz \;/\; \max(A_2)$.

(c) by accepting elimination of higher azimuthal order fields in a z–integrated sense, *i.e.*

$$\int_{-\infty}^{+\infty} dz \int_{-\pi}^{+\pi} d\theta\, A_z\,(r,\theta,z)\,\cos\,(4l+2)\,\theta = 0 \quad \text{for} \quad 1 \le l \le NH \tag{3}$$

Here A_z refers to the z component of the vector potential produced by an *individual* quadrupole magnet and NH is the index of the maximum overtone of concern (generally three or less). Presuming time-independent currents, one may show that the previous condition is equivalent to

$$\int_0^L dz \int_0^{2\pi} d\theta\,\cos\,(4l+2)\,\theta \int_0^{R_{max}} dr\, r^{-4l-1}\,\mathcal{J}_z\,(r,\theta,z) = 0 \quad \text{for} \quad l \neq 0 \tag{4}$$

where R_{max} is the maximum radial extent of the current windings. For all of the designs discussed in this note, the windings lie on one or at most two cylindrical surfaces of constant radius. Hence, we will replace the integral over r of the current volume density $\mathcal{J}_z$ by the equivalent surface current density J_z.

A. Laslett-Brady-Celata-Faltens (LBCF) design

Following Falten's suggestion that ILSE use pulsed, iron-free electromagnets with extremely compact ends, L.J. Laslett [1] studied a short quad design composed of straight windings in z (*i.e.* at constant θ) whose ends were connected by circular arcs in θ at constant z, all lying on a cylindrical surface (or two if more than one layer of turns was necessary). The developed view of such windings is a set of nested rectangles. For simplicity, the wire leads to and from the external world were ignored. V. Brady [5] determined the optimal azimuth positions θ_k that satisfied Eq. (4). Although this design cannot be constructed exactly with existing superconducting cables (due to the infinitesimally small radii of curvature at the end of the straight sections), it is an "instructive" design in that it probably best satisfies the above points (a) and (c) for a given a_{wire}.

As explained in Ref. 5, Eq. (4) must be replaced by

$$\sum_{k=1}^{NW} L_k\,\cos\,(4l+2)\,\theta_k \;=\; 0 \quad \text{for}\; l = 1,2,...,NH \tag{5}$$

where L_k is the (specified) length of the kth wire, NW is the number of wires per quadrant (8 or 12 generally being chosen in this study), and the azimuthal positions θ_K are to be determined. When $NH < NW$, the set of θ_k that satisfy

relation (5) is not unique and additional conditions must be applied. Laslett suggested a Lagrangian multiplier scheme where the function

$$\psi = \sum_{k=1}^{NW} (\theta_k - \varphi_k)^2 + \sum_{l=1}^{NH} \frac{F_l}{(4l+2)} \left[\sum_{k=1}^{NW} L_k\,\cos\left((4l+2)\,\theta_k\right)\right] \tag{6}$$

must be minimized. Differentiating ψ with respect to θ_k gives the necessary second constraint

$$2\,(\theta_k - \varphi_k) - \sum_{l=1}^{NH} F_l\,L_k\,\sin\,(4l+2)\,\theta_k \;=\; 0 \quad k = 1,2,...,NW \tag{7}$$

Differentiation with respect to the Lagrangian multipliers F_l returns expression (5). The φ_k in Eq. (7) are constants which Laslett and Brady set equal to the distribution

$$\varphi_k \equiv \frac{1}{2}\,\sin^{-1}\left(\frac{k-1/2}{NW}\right) \quad \text{for } k = 1,2,...,NW \tag{8a}$$

In the limit $NW \to \infty$, this choice of φ_k results in a $\cos 2\theta$ current distribution azimuthally. Another possible choice (not tested as of yet) would be to replace the first summation in Eq. (6) by

$$\sum_{k=1}^{NW} (\theta_k - \theta_{k-1})^2 \quad \text{for } k = 1,2,...,NW \tag{8b}$$

which would try to force the wires to be spaced as uniformly as possible. This choice is attractive from a mechanical point of view because it prevents the epoxy spacers between the individual wires from becoming too small.

A simple VAX Fortran code ("FILLY") used by Brady was adapted easily to SUN Fortran-77. Both the VAX and SUN versions use the core IMSL subroutine DNEQNF to solve Eqs. (5) and (7) simultaneously via the Levenburg-Marquardt algorithm using a finite difference Jacobian. In certain circumstances with $NH \ge 4$, the algorithm will not converge; Brady also encountered this difficulty. We overcame the problem by first solving the equations by setting $NH = 2$, using the derived θ_k to reset the φ_k, and then solving $NH = 3$ and so on in a bootstrap manner up to the desired order (generally $NH = 5$ or 6). For $NW = 8$, FILLY typically required less than 2 CPU seconds on a SUN-4/25 workstation.

Once the wire positions were determined, we used the MAFCO code to calculate via the Biot-Savart law the magnetic field at specified locations. Since

our interest was in determining the vector potential as a function of z through r^6 (thus including the dodecapole and pseudo-dodecapole components), we first calculated B_θ on a uniform z-grid at 3 radial positions *e.g.* r_{low}, r_{mid}, r_{high}. In general we set $r_{low} \leq 0.1a_{wire}$, $r_{high} = 0.8a_{wire}$, and $r_{mid} = \sqrt{r_{low}r_{high}}$. The following algorithms determine $A_6(z)$, $A_2(z)$, $A_2''(z)$, $A_2^{iv}(z)$:

$$A_6(z) \equiv \frac{1}{3}\,\frac{2B_\theta(r_{high},30^\circ) - B_\theta(r_{high},30^\circ)}{6r_{high}^5} \tag{9}$$

and

$$\left[A_2r^2 - \frac{1}{12}A_2''r^4 + \frac{1}{384}A_2^{iv}r^6\right] \equiv -\frac{r}{3}\left[B_\theta(r,0^\circ) + B_\theta(r,30^\circ)\right] \tag{10}$$

When evaluated at a given z for each of the three radial positions, Eq. (10) produces a set of three simultaneous equations which can be solved easily for the three components of A_2. An alternative method is to determine $A_2(z) = -[B_\theta(r,0^\circ) + B_\theta(r,30^\circ)]/3r$ at a single $r \ll a_{wire}$ and then numerically differentiate the resulting answer with respect to z to obtain the other wanted components, A_2'', A_2^{iv}. We found this method to be numerically noisy, especially for A_2^{iv}, and prefer the radial expansion used in Eq. (10).

At this point we must convert our results for A_2, *etc.* for a single, isolated magnet into the values corresponding to a periodic lattice in z. We followed a "brute force" approach by writing a simple Fortran code ("XLATTICE") to calculate

$$f_{lattice}(z) = \sum_{n=-\infty}^{+\infty}(-1)^n f_{iso}(z+nL) \approx \sum_{n=-2}^{+2}(-1)^n f_{iso}(z+nL) \tag{11}$$

where f_{iso} represents the values previously calculated for a single magnet. Since $A_2(z)$ falls off as z^{-5} for $|z| \geq 2a_{wire}$, the cutoff in the summation introduces very little error. The XLATTICE code stores the lattice values of A_2, A_2'', A_2^{iv}, A_6 in an ASCII file which can then be read by a simulation code such as HIFI.

The above procedures were quite successful in removing the z-integrated multipoles as desired; generally

$$\int_0^L A_6(z)\,dz < 0.01\int_0^L |A_6(z)|\,dz \tag{12}$$

as determined numerically for the periodic lattice with $\Delta z \approx 0.02L$. One must recognize, however, that the above design procedure leads to expression (3)

being strictly true for an isolated magnet only. As a_{wire}/L increases, the z-extent of the fringe fields grows larger. Consequently, there can be partial cancellation of adjacent fringe and multipole fields and their z-integrals over a half-lattice period L will begin to deviate from zero (although over the full lattice period of $2L$, the integrals will remain zero).

B. Laslett-Caspi-Helm (LCH) Design

These authors [4] delineated a procedure for designing coil ends of dipole magnets that had no overtones in the z-integrated sense (*c.f.* Eq. (3)). The end windings (and straight sections if any) all lie on a cylinder of constant radius ($\equiv a_{wire}$). If we denote $y = a_{wire}\sin\theta$ as the vertical transverse coordinate with $0 \leq \theta \leq \pi/2$, LCH found that when individual coil end wires followed the analytic relation

$$z(y,y_0) = f(y_0) - f(y-y_0) \quad , \tag{13}$$

the field would be as desired. Here y_0 identifies the individual wire and refers to the y coordinate of the straight (*i.e.* y=constant) portion of the wire, while f is an arbitrary analytic function. In the coil end portions, y smoothly increases from y_0 to a_{wire} at its maximum extent in z. To extend this procedure to quadrupole magnets in which $0 \leq \theta \leq \pi/4$, the actual vertical transverse coordinate remains equal to $a_{wire}\sin\theta$ but the y and y_0 used in Eq. (13) are now proportional to $\sin 2\theta$.

LCH paid particular attention to terminations defined by the relation $f(y) = \zeta a_{wire}(y/a_{wire})^p$ where ζ and p are constants. With this formulation, the maximum extent of the curved ends beyond the straight section is

$$\begin{aligned}|z(a_{wire},0) - z(a_{wire},a_{wire})| &= |f(0) - f(a_{wire}) - f(a_{wire}) + f(0)| \\ &= 2\zeta a_{wire}\end{aligned} \tag{14}$$

and is thus p-independent for $p > 0$. The special case of $p = 1$ reproduces the Lambertson-Coupland termination which had been suggested for the ESCAR project here at LBL; the $(y-z)$ projections of the ends are straight lines. As p decreases to 0^+, the windings at large y_0 terminate earlier and earlier in z, and the magnet end becomes more compact in an average sense (although as $NW \to \infty$, the maximum z extent of the last winding at $y_0 = 0$ remains unchanged).

We concentrated on designs with $p = 0.25$ and 0.5, and $\zeta = 1.0$. Designs with smaller p are quite similar to the LBCF magnets of the previous section whereas the Lambertson-Coupland end with $p = 1$ has a right angle bend at $y = y_0$ which presents mechanical difficulties for superconducting cable. We set the number of wires per quadrant to 12 and solved for the azimuthal

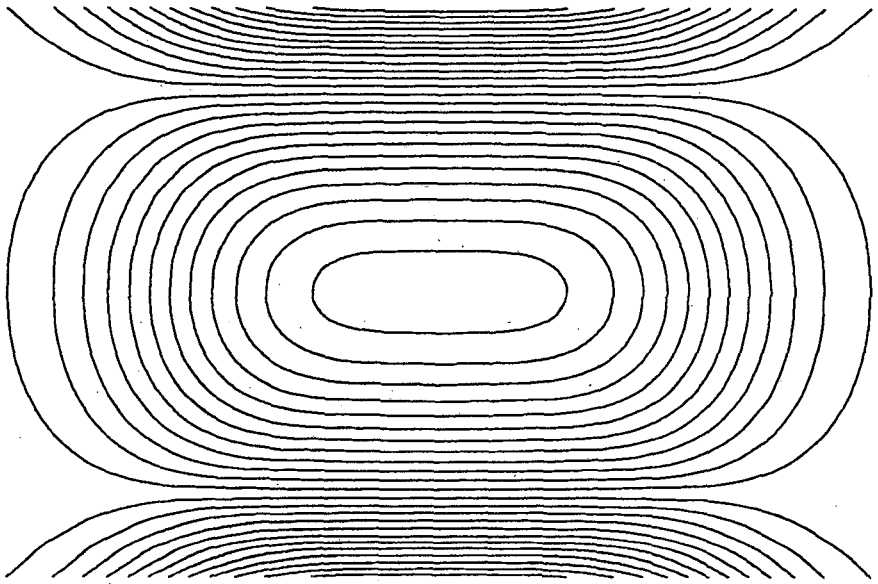

Figure 1: A top $(x - z)$ view of a half-period of an LCH magnet with $p = 0.25$, $\zeta = 1.0$ and no "straight" section. $L_{wire}/a_{wire} \approx 4$ in this case.

positions y_0 using an appropriately modified version of FILLY. Usually, the resultant wire positions produced a field topography with $|\int_0^L A_6(z)\,dz| < 0.025 \int_0^L |A_6(z)|\,dz$ or less for a 10-mm step size in z. In the absence of any purely "straight" section between the magnet ends (as was true in this study - the LCH magnets are just two coil ends stuck together), the y_0's are functions of p only and are independent of ζ and a_{wire}. A top view of the wire configuration of an LCH magnet with $p = 0.25$ and $\zeta = 1.0$ is shown in Fig. 1.

The relatively complicated curved ends of the LCH magnet designs presents some difficulties when calculating the expected magnetic field. Although in theory MAFCO can do such calculations by subdividing each curved end into many short chords, we found chose an alternative approach of calculating B_θ by using magnetic scalar potential theory as implemented in a new code named "XSQUAD". As shown in Appendix A, if a closed current loop of arbitrary shape lies on a cylinder of constant radius, one may subdivide the loop azimuthally into a large number N of closed rectangular microloops (or equivalently, to replace the curved boundary by a staircase approximation). One can then determine B_θ analytically and then extract the various multipoles and pseudo-poles in a straightforward fashion.

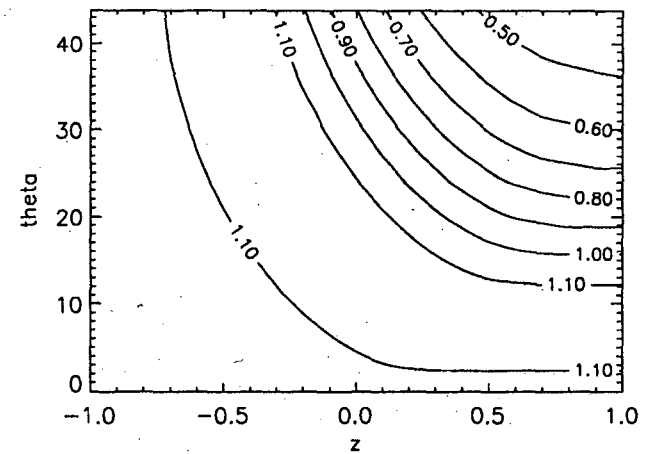

Figure 2: Contour map of the wire radius of curvature for an LCH termination with $\zeta = 1.0$ and $p = 0.5$; the values are normalized to a_{wire}. For plotting purposes, values at $z \geq z(y_0, y_0)$ (where the wires are at constant θ) were set equal to the computed value at $z(1.02 * y_0, y_0)$ rather than the actual value of infinity. The magnet pole tip is at $\theta = 45°$ while the center of the magnet is at $z \geq 1.0$.

Apart from multipole suppression, the terminations must also have a reasonably large radius of curvature ($\equiv R_c$) to permit use of superconducting cable. For wires that lie on a cylinder of radius R and follow a curve denoted $z(\theta)$,

$$R_c = \frac{\left(R^2 + z'^2\right)^{3/2}}{R\left(R^2 + z'^2 + z''^2\right)^{1/2}} \tag{15}$$

where the primes refer to differentiation with respect to θ. For constant $z(\theta)$, $R_c = R$ as expected while for z'=constant, $R_c = (R^2 + z'^2)/R > R$ showing that drawn-out ends with a small z'' can actually increase R_c to larger than the cylinder radius.

Fig. 2 shows a contour map of the radius of curvature (normalized to a_{wire}) for an octant of an LCH magnet end with $\zeta = 1.0$ and $p = 0.5$. For this particular configuration, the minimum value of $R_c \approx 0.5\,a_{wire}$; this minimum appears to scale inversely with ζ (or equivalently the length of the magnet ends) in the range $0.25 \leq \zeta \leq 1.0$. Since $a_{wire} \geq 60$ mm for most HIF transport lattices, it appears likely that LCH or similar terminations can be wound with superconducting cable without fear of running into radius of curvature problems.

C. "Nested Ellipse" Design

Although the LCH coil ends of the previous section are probably more than adequate for ILSE purposes, they may have certain undesirable properties. First, simulations of transport with $p \approx 0.5$ showed beam particles at large radii displaying an unstable resonance (at small amplitudes) caused by simultaneous interaction with the dodecapole and AG flutter motion due to the quadrupole fields. The resonance is manifested by emittance growth and can lead to particle loss. The resonance strength depends both on the geometry of the coil ends and the degree of tune depression. For typical ILSE parameters with $\sigma_o \gg \sigma$, the resonance is quite weak and should pose no problems. Second, despite the present availability of CAD/CAM systems, the analytic formulation of the LCH ends might prove problematic in actual implementation, and we hoped that simpler curves might be possible.

One such design is termed the "Nested Ellipse" coil end. This design is in many ways a hybrid of the original LBCF ILSE design but, in place of right-angle turns, this design employs curved, elliptical ends that are nearly identical to LCH coil ends when $p = 0.5$. Mathematically, the ends are described as follows:

Let k index the wires and θ_k^0 be the azimuthal angle of the straight portion (*i.e.* $\theta_k(z)$ =constant) of the wire in a given octant. The θ_k^0 will be close to the φ_k of expression (8a) for NW large. The length of the straight portion of each wire is set to be

$$z_k^s \equiv z_1^s + (k-1)\,\Delta z_{inc} \tag{16}$$

while curved end obeys the following law:

$$z\left(\theta_k^0 \le \theta \le \pi/4\right) = z_k^s + z_{curve} \times \sqrt{1 - \left(\frac{\pi/4 - \theta}{\pi/4 - \theta_k^0}\right)^2} \tag{17}$$

In the developed view, the curved ends are a set of half-ellipses whose centers in z are offset by $(k-1)\Delta z_{inc}$. The parameters Δz_{inc}, z_{curve}, and z_1^s are free to be chosen by the designer; the magnet's effective length will be most sensitive to the last parameter. We again modified the FILLY code to produce the optimum θ_k for a given specification of these three parameters and NW. Fig. 3 shows a top view of such magnet with parameters similar to those used for the ILSE test magnet currently under construction. This magnet has an $\approx 20\%$ longer effective length (normalized to a_{wire}) than the LCH magnet of Fig. 1.

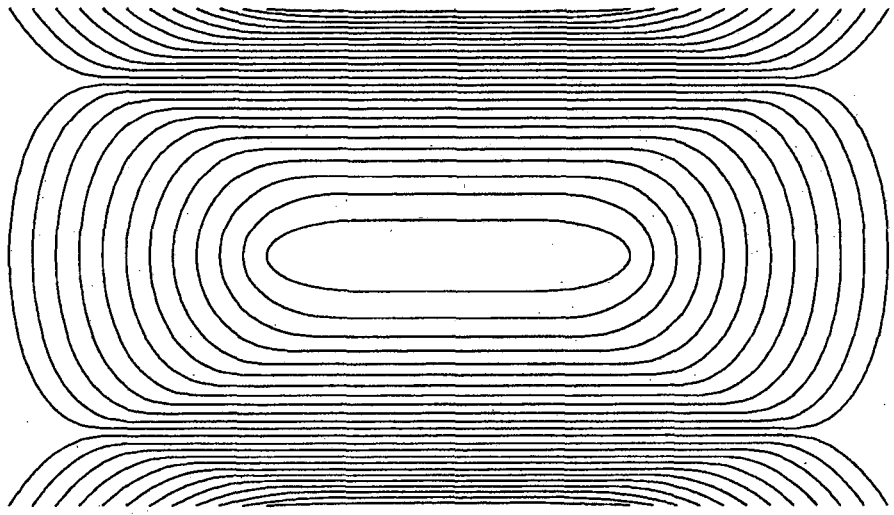

Figure 3: A top view of the wire configuration for a half-period of a "nested ellipse" quadrupole magnet. For this case $\theta_k = \varphi_k$ [see relation (8)a], $a_{wire} = 82.5\,\text{mm}$, $z_s^o = 30\,\text{mm}$, $z_{curve} = 32\,\text{mm}$, and $\Delta z_{inc} = 8\,\text{mm}$.

D. Laslett "Fourier-Bessel" Magnet

Midway during the course of this study, Dr. Laslett introduced us to a class of a magnets that are "pure" quadrupoles in the azimuthal sense. His interest germinated from the nature of the general solution to the Laplacian in cylindrical coordinates. As we became more familiar with the mathematics of this solution, we realized that it contained the topographical essence of large aperture quadrupole magnets.

Based on solutions to the Laplacian, the mathematical representation (interior to the wires) of a periodic, scalar magnetic potential Φ_m with a pure quadrupole symmetry must resemble

$$\Phi_m(r,\theta,z) = \sin 2\theta \sum_{n=1,2,3,\ldots}^{\infty} \alpha_n\, I_2\left(\frac{n\pi r}{L}\right) \cos\left(\frac{n\pi z}{L}\right) \tag{18}$$

where I_2 is the normal modified Bessel function. If we restrict our attention to FODO lattices whose current-carrying wires are at a single radius a, then

$$\Phi_m(r,\theta,z) = \frac{\mu_0 a}{2} \sin 2\theta \sum_{n=1,3,5,\ldots}^{\infty} \alpha_n \left[\frac{n\pi a}{L}\right] K_2'\left(\frac{n\pi a}{L}\right) I_2\left(\frac{n\pi r}{L}\right) \cos\left(\frac{n\pi z}{L}\right) \tag{19}$$

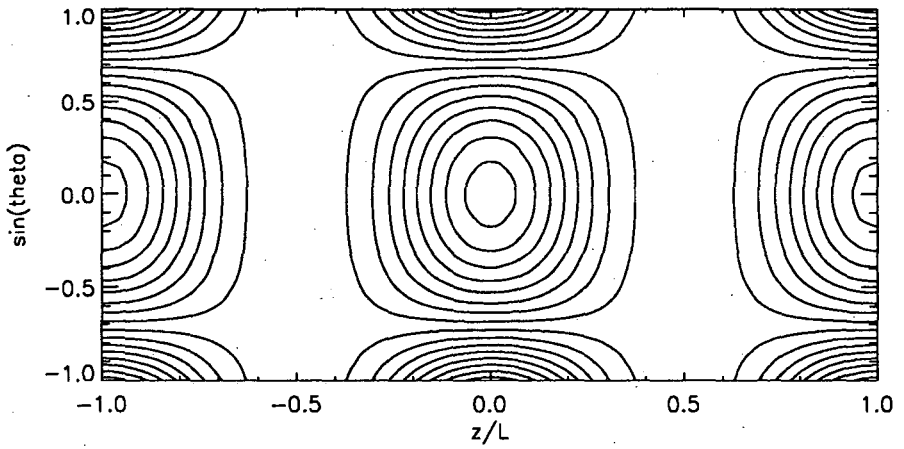

Figure 4: Top view of the 8-wire configurations for a "two-term" Fourier-Bessel magnet. The wire positions are contours of constant $\vec{h}$ as given in expression (21).

and the surface current

$$\vec{J}(\theta,z) = \sum_{n=1,3,5\ldots}^{\infty} \alpha_n \left[\cos\left(\frac{n\pi z}{L}\right)\cos 2\theta\,\vec{e}_z + \frac{n\pi a}{2L}\sin\left(\frac{n\pi z}{L}\right)\sin 2\theta\,\vec{e}_\theta\right] \quad (20)$$

This choice of surface current is divergence-free and one may show that

$$\vec{J}(\theta,z) = \nabla\times\vec{h} \quad \text{with} \quad \vec{h} = -\vec{e}_r\,\frac{a}{2}\sin 2\theta \sum_{n=1,3,5,\ldots} \alpha_n \cos\left(\frac{n\pi z}{L}\right) \quad (21)$$

The current flow lines are contours of constant $\vec{h}$ (much as magnetic field lines are lines of constant $\vec{A}$). Therefore, regions with high current density (or, equivalently, lots of tightly spaced windings) occur where $\vec{h}$ changes rapidly. Conversely, regions of nearly constant $\vec{h}$ are sparsely populated with wires.

Since one has total freedom in picking the Fourier coefficients α_n, one can tune the wire configuration toward a particular geometrical goal or, on the other hand, tune the on-axis field toward a particular profile in z. Note that for $\zeta \geq 1$, $I_2(\zeta)$ increases and $K_2'(\zeta)$ decreases nearly exponentially with ζ. This causes the filed contributions of terms with larger n in expression (19) to be relatively larger near the wire radius than on-axis, and, as a increases, the on-axis field becomes increasingly dominated by the fundamental ($n = 1$) Fourier component.

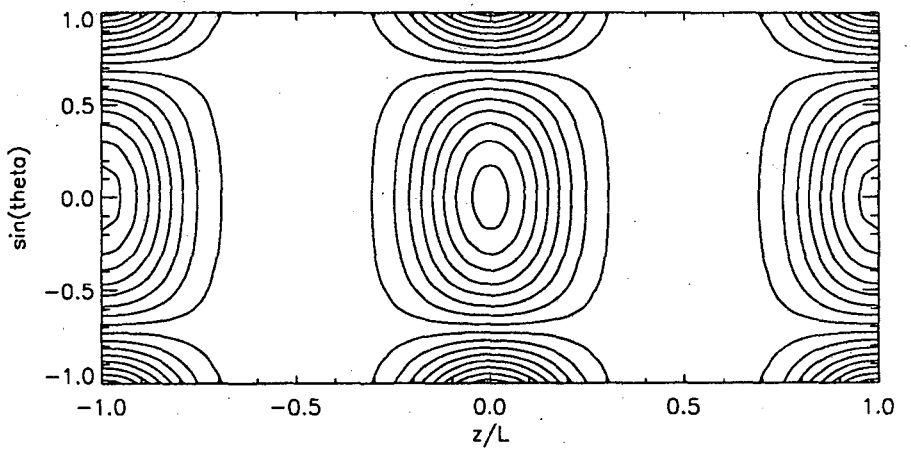

Figure 5: Same as Fig. 4 but for a "three-term" magnet. Compared to the "two-term" magnet. one sees a significant increase in the open space between the F and D windings but at a price of decrease effective length.

In order to adapt these Fourier-Bessel magnets to a "real" induction accelerator which requires winding-free gap regions, we can open up the spacing between windings in longitudinal regions centered upon $z/L = \frac{1}{2}, \frac{3}{2}, \frac{5}{2}, \ldots$ by picking appropriate values of $\alpha_1, \alpha_3, \alpha_5, \ldots$ to force h to be constant with z in these regions. For a "two-term" magnet (*i.e.* α_1 and α_3 are the only non-zero values), one finds that if $\alpha_1 = 1$ and $\alpha_3 = 1/3$, the first (and second) z-derivatives of $\vec{h}$ are eliminated at $z/L = \frac{1}{2}, \frac{3}{2}, \frac{5}{2}, \ldots$. This choice is also equivalent to making $\vec{h} \propto \cos^3(\pi z/L)$ and $J_\theta \propto \cos^2(\pi z/L)$. As shown in Fig. 4, the open space in a 8-wire quadrupole is about $0.25L$. To further increase the opening to about $0.36L$, one may use three-term expansion with $\alpha_1 = 1$, $\alpha_3 = 0.5$, and $\alpha_5 = 0.1$; in this case, $\vec{h} \propto \cos^5(\pi z/L)$. One pays a price of decreased effective length for these openings: the effective length for the two- and three-term magnets being 0.67 and 0.55 of that corresponding to a one-term magnet for a/L small.

Since the magnetic field $\vec{B} \equiv -\nabla\Phi_m$, we used expression (19) to evaluate $\vec{B}$ analytically for the simulation code results of the next section. This solution is the limiting case for a constant lattice (in both L and peak $\vec{B}$) of infinite length with an infinite number of wires per individual quad. In actual practice, the fields in the first and last couple of lattice periods will deviate somewhat from this solution. There will also be only a finite number of current-carrying wires in each quadrant and one must also consider the fields due to wire leads

to and from each half-period. Moreover, most realistic lattice designs for HIF drivers have both L and the peak $\vec{B}$ varying slowly with z. All these subtleties should be considered when modeling the fields in an actual lattice.

III. Particle Simulation Transport Results

For any particular magnet design, a critical question is the size of its useful dynamic aperture over the needed beam transport distance. We conducted a number of transport studies with the HIFI simulation code to obtain an answer. Because HIFI follows only a single, transverse slice and makes various approximations for the external and internal (*i.e.* space charge) fields (see Appendix B for details), it is a relatively fast-running code. In collaboration with I. Haber, a number of runs with the more complex (and slower) SHIFTXY code were made to check the accuracy of HIFI results. In general we found that HIFI could predict emittance growth over 300 m or less to accuracies of a few per cent, the uncertainty being reduced with a larger number of simulation macroparticles.

A. General Simulation Characteristics

Nearly all of the magnet lattices used in these simulations had a half-period $L = 0.5$ m (corresponding to the present conceptual design of the ILSE magnetic transport section) and clear beam pipe radii ranging from 60 to 200 mm. The external fields were discretized on a $\Delta z = 10$ mm grid and expanded through r^5 or higher using the algorithms of Eqs. (9) and (10). The particle-mover step size was generally 10 or 5 mm with simple linear interpolation of the external fields done when necessary.

Although HIFI has the capability of simulating acceleration in induction gaps, these particular runs were done at constant energy. Furthermore, the ILSE transport simulations adopted the paraxial approximation with both v_z and the time step kept constant (for $\sigma_o \approx 72°$ and $a_b/L \approx 1/10$, v_z varies by about ± 1 part in 400 due to flutter motion). We generally offset the beam centroid by a small amount ($\leq 10^{-2} a_{beam}$) in order to simplify measuring σ_o by examining $\bar{x}(z)$ plots. Both RMS emittance and particle loss were continuously monitored as the most important measures of beam quality. The beam pipe walls were made perfectly absorbing for incident macroparticles. For ILSE runs, the simulated transport distances were 60 meters - long enough to permit the beam to reach a new equilibrium and display rapid particle loss, if any.

B. ILSE-type magnet simulations

The magnetic transport section of ILSE must transport a single beam of K^+ at $1.0\,\mu$C/m line charge density at an initial energy of $\approx$4.5 MeV. A lattice period of 1.0 m has been adopted, equal to that of the 4-beam combiner immediately upstream. The expected beam normalized emittance after beam merging lies

in the range $3 - 20 \times 10^{-6}$ m-rad, which implies a space charge-depressed tune ratio σ_o/σ of $\sim 2.5 - 10$ for $\sigma_o \approx 72°$. For these parameters, the matched beam radius lies in the range 40-60 mm or, equivalently, $L/a_{beam} \sim 8 - 12$. This aspect ratio is large enough that one is nearly certain that numerous magnet designs should be possible without the beam exceeding the dynamic aperture. To examine the effects of anharmonic fringe fields, we have concentrated on designs with $L_{wire}/a_{wire} \sim 3 - 4$ with $a_{wire} \sim 82.5$ mm. Here L_{wire} is the maximum longitudinal extent of the wires in each half period.

Our first ILSE example is an "LBCF" magnet whose wires lie in 2 radial layers, each containing 8 turns, at 80 and 85 mm radius, and whose straight wire lengths range from 0.21 to 0.24 m. The quadrupole's effective length is 0.209 m and a σ_o of 72° requires a field gradient of 18.6 T/m for 4.5 Mev Ne^+ (most of the ILSE simulations were done when Ne^+ was the leading ion candidate for ILSE; even after it was replaced by K^+, we continued its use for purposes of comparison). This leads to a matched beam radius of 38 mm for $\lambda = 1\,\mu$C/m. The AG flutter motion causes the radius to vary from 28 to 49 mm. We adopted a relatively low normalized emittance, 3.3×10^{-6} m-rad, which depressed the tune to $\sigma \sim 6.9°$. Over the 60-meter transport distance, the beam emittance increased a few percent (see Fig. 6) the full current survived without any loss. As displayed in Fig. 7, the beam shape remained nearly elliptical although the $x - x'$ and $y - y'$ phase space projections developed mild butterfly shapes at $z = 18.25$ m. When the initial particle lad follows a KV distribution, the $x' - y'$ phase space shows an extensive hollowing - this takes about 10 m to develop and persists for about another 15 m of transport after which a mild halo appears in velocity space. The hollowing is due to the outermost particles in configuration space (and equivalently innermost in velocity space) heating up due to nonlinear fields. Such hollowing does not develop in an identical simulation using a beam with a semi-Gaussian distribution although the final emittance growth was also a couple per cent.

Dropping σ_o to 45° by letting $B' \rightarrow 12.1$ T/m led to the matched beam radius growing to 58 mm and the maximum radius due to flutter extending out to 69 mm. The emittance then grew by $\sim 20 - 30\%$ over 60 m of transport and butterfly shapes in the $x - x'$ phase spaces were far more extreme. Transverse velocity phase space plots again show hollowing by development further in z of a mild halo consisting of $\sim 10\%$ of the beam particles.

Doubling the beam line charge to $2.0\,\mu$C/m and the normalized emittance to 6.6×10^{-4} rad-m while keeping σ_o constant at 72° produces the same growth in matched beam size as the aforementioned $\sigma_o = 45°$ case but somewhat smaller emittance growth, $10 - 12\%$. The small clearance to the pipe walls

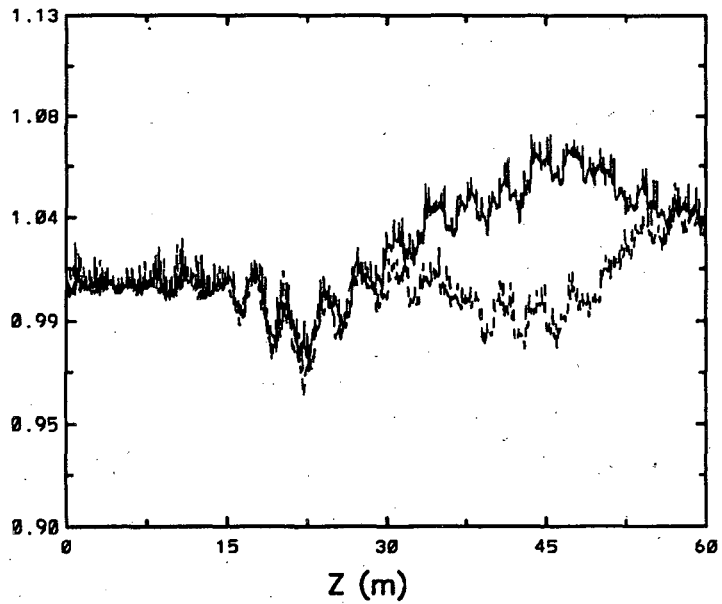

Figure 6: RMS emittance vs. z for an ILSE-like beam over 60 m of transport through an LBCH magnet lattice with $\sigma_o = 72°$ and $\sigma = 7°$. The plotted values are normalized to the initial starting value with the solid and dashed curves referring to the $x - x'$ and $y - y'$ planes respectively.

at $r = 75$ mm led to a $1 - 2\%$ current loss over the 60-m transport distance. We attribute this loss to the scraping off of a very minor halo as opposed to the beam size exceeding the true dynamic aperture of the magnet [which is $O(140\,\text{mm})$ for these parameters – see §IV-B].

A series of run with "LCH" magnets with $p = 0.5$ and $\zeta = 1.0$ showed similar behavior. The ILSE base case of $\sigma_o = 72°$ and $\lambda = 1.0\,\mu\text{C/m}$ displays a minor butterfly shape development in $x - x'$ phase space and a small ($\sim 5\%$) emittance increase. The somewhat shorter effective length, 0.176 m, relative to the LBCF magnets results in the need for higher peak field gradients (21.8 T/m versus 18.6). As σ_o is reduced to 45°, the maximum beam radius increases to just under 70 mm and the emittance grows by $\sim 33\%$, with just a tiny amount of particle loss occurring to the walls over the last 5 m of transport. A final simulation with $\lambda = 2.0\,\mu\text{C/m}$ showed $\approx 15\%$ emittance growth and 4% particle loss. As before, this loss is not a dynamic aperture effect but rather the result of the small initial clearance between the beam pipe and the maximum beam envelope.

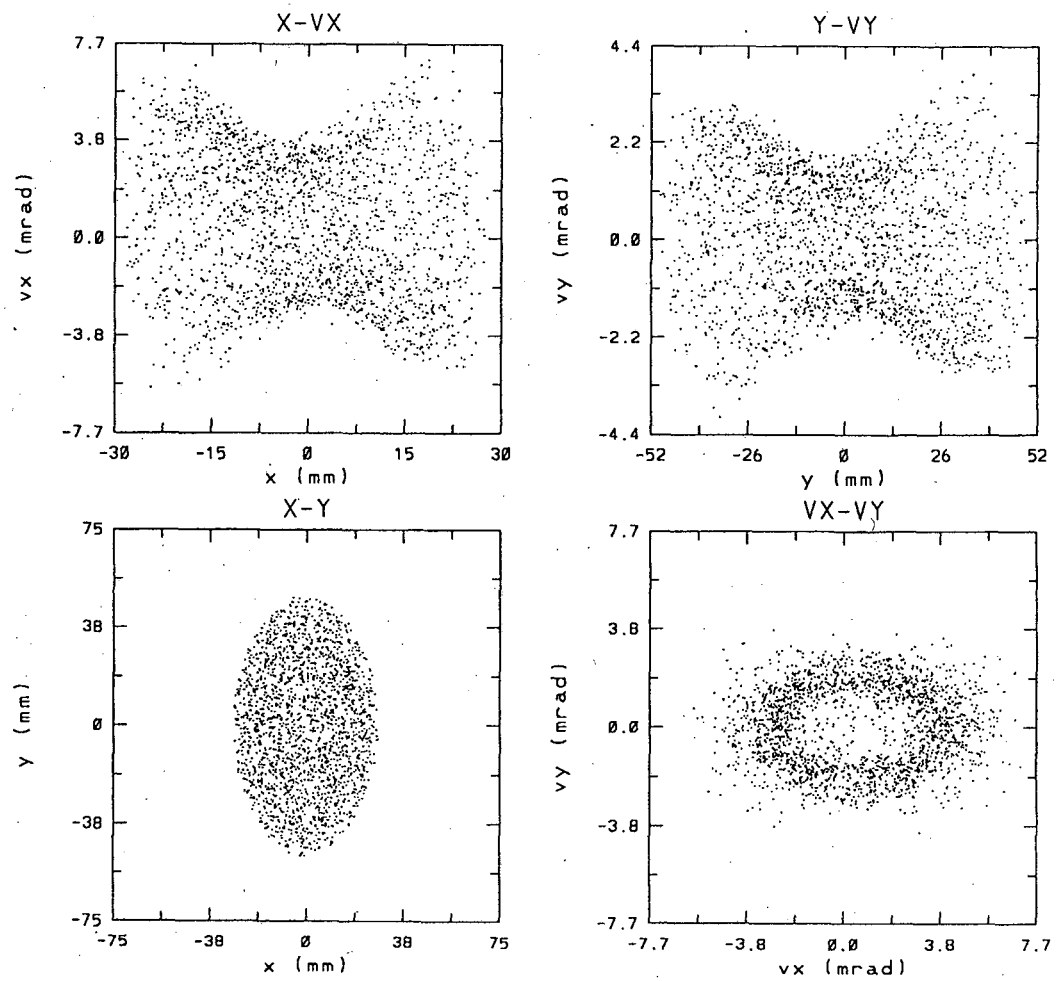

Figure 7: Configuration and phase space snapshots of an $1\mu\text{C/m}$ ILSE-like beam in an "LBCF" magnet after 18.25 m of transport. The initial particle load was a KV distribution.

We also studied a second LCH magnet with $p = 0.25$. The reduction in p leads to less extended (on the average) curved ends and an even shorter effective length, 0.169 m. Nonetheless, the transport properties for $\lambda = 1.0\,\mu$C/m remain similar: a small emittance increase when $\sigma_o = 72°$ and a 35% increase for $\sigma_o = 45°$. Transport of a $2.0\,\mu$C/m beam results in a greater emittance increase (50%) but somewhat less particle loss than for the corresponding run with the $p = 0.5$ magnet.

Transport simulations through nested ellipse ILSE magnets show nearly identical behavior to that corresponding to the LCH magnets. The defining parameters for these magnets were chosen to be the same as the ILSE "materials-test" magnet prototype: 12-wires/layer, $a_w = 82.5$ mm, 60-mm straight section, $\Delta z_{inc} = 8$ mm and 32-mm curved ends (see expressions (16) and (17)). The magnet has an effective length of 0.215 m, a total wire length of 0.3 m, and about 45:1 suppression of the integrated dodecapole moment. A $1.0\,\mu$C/m Ne^+ beam with a maximum envelope size of 49 mm, $\sigma_o = 72°$ (B' =18.35T/m), and $\sigma = 7°$, propagates the 60-m simulation distance with less than a 3% increase in emittance. When the line charge density is increased to $2.0\,\mu$C/m (with a maximum envelope size of 70 mm), the final emittance increase is about 7% and the current loss is quite small($\leq$2%), despite the closeness of the beam pipe wall at 75 mm. The $x - x'$ and $y - y'$ phase spaces exhibit mild butterfly shapes and a slight halo forms in velocity space, as was true for the LHC magnets discussed in the previous paragraph. A final run with $\lambda = 1.0\mu$C/m but σ_o decreased to 45°, giving a maximum beam radius of 69 mm, results in a 20% emittance increase, with nearly all of this due to a small fraction ($\sim 10 - 20\%$) of the particles forming a halo in velocity space. There was no particle loss over 60 m despite the emittance increase.

Given the relative ease of beam transport and lack of strong emittance growth for these various ILSE cases with $L/a_{wire} \geq 6$, we decided to study a more stressing set of parameters by decreasing L to 0.4 m and increasing a_{wire} to 100 mm. The dimensions of the straight and curved end portions of the windings were increased proportionally with a_{wire} resulting in L_{eff} increasing to 0.281 m. Since the proposed ILSE Metglas cores will be wound in 0.1-m longitudinal lengths, such a decrease in L is physically possible, although there would be less length available for diagnostics and overhang of an iron yoke (if used). For $\sigma_o = 72°$ and $\lambda = 1.0\,\mu$C/m, the new equilibrium beam size decreased to 30 mm from 38 mm. The corresponding field gradient is 20.6 T/m. The emittance growth for this base case remains under 3% for a 60-m transport distance. Increasing λ to $4.0\,\mu$C/m (and a_b to 61 mm) while keeping σ_o and σ constant results in an emittance increase of $\approx$ 20% and a tiny (1-2%) current loss, even though the maximum beam radius, 78 mm, is $\approx$ 20% of the magnet half-period.

Due to expected limits both on the ILSE injector perveance and on the focusing strength in the electrostatic transport section, reducing σ_o at a fixed L is probably the most realistic way to expand the beam size in order to test the effects of magnetic focusing nonlinearities. Keeping λ constant at $1.0\,\mu$C/m but decreasing σ_o to 45° and σ to 3.1° leads to a_b growing to 47 mm and again a 20% emittance increase. A further decrease of σ_o to 30°, σ to 1.4° and increase of a_b to 69 mm and maximum beam radius of 77 mm produces strong phase space distortions in the first 15 m of transport, a doubling of the emittance by $z = 60$ m, but again no current loss within the 90-mm beam pipe wall. However, even these larger beams do not allow ILSE to test limits on transport without particle loss because as σ_o decreases, the dynamic aperture also increases (see § IV-B).

Our last set of ILSE simulation runs were done with the Fourier-Bessel magnet topography proposed by Laslett. Once σ_o and the half-lattice period L are chosen, there are really only two free parameters: the wire radius a_{wire} and the relative sizes of the different Fourier components α_n [see Eq. (19)]. We examined two different geometries: 1) a fundamental-only magnet with the magnetic field varying in z as $\sin(\pi z/l)$ 2) a "three-term" magnet consisting of the fundamental and the first two overtones whose coefficients were picked to maximize the "open space" between the F and D windings.

As expected from the lower effective length of the three-term magnet, the required field at a_{wire}, 1.76 Tesla, to make $\sigma_o = 72°$ for 4.5 MeV Ne^{+1} was significantly larger than that corresponding to the one-term magnet, 1.08 Tesla. Both magnets could transport beams of up to $1.5\,\mu$C/m line charge density without loss to the walls at 70 mm. The three-term magnet had larger emittance growth, 10% versus 5%, for the $\lambda = 1.5\,\mu$C/m, presumably due to the larger fringe fields associated with A_2'' term of expression (2).

C. Limits on σ_o

The results of the previous section indicate that many quadrupole magnet designs can be used in ILSE to transport with particle loss or significant ($\geq$ 10%) emittance growth $1.0\,\mu$C/m of Ne^+ in a 1.0-m FODO lattice with $\sigma_o = 72°$. A related issue is the permitted range of σ_o. In many instances, an HIF beam will have a time-varying velocity "tilt", with the longitudinal velocity at a given z increasing from the beam head to the beam tail. This tilt serves to compress the beam in time, and, in some cases, in space as it accelerates. For ILSE, velocity tilts as high as 25% have been proposed near the front end of the accelerator, although nearly all HIF driver scenarios use far smaller tilts. In the magnetic

focus section, $\sigma_o \propto v_z^{-1}$; thus, the head will have a larger σ_o than the nominal value at the beam mid-point, while the beam tail will have a correspondingly lower value.

As σ_o increases, the beam size decreases proportionally (presuming a constant line charge density) and the effects of anharmonic focusing decrease. On the other hand, as σ_o passes 90°, the beam enters into a region of envelope instability. From a *theoretical* viewpoint, there are bands of instability that appear for $\sigma_o \geq 100°$ on a σ versus σ_o plot as shown by Hofmann *et al.* [6](see their Fig. 6 in particular). From an *experimental* viewpoint, Tiefenback's [7-8] work with SBTE showed unstable beam envelope growth for $\sigma_o \geq 88°$ at low values of σ. Thus, a conservative design would keep σ_o below 85°, although there may be isolated, stable operating regions as high as 105°. For a nominal σ_o of 72° at mid-beam, the 85° criterion permits a center-to-head decrease in v_z of 18%.

As σ_o decreases, the equilibrium beam size increases for constant line charge density. It becomes more difficult to match the beam since the relative strength of the nonlinear focusing terms increases with r, and, if σ_o becomes too low, there will be beam loss on the pipe walls. Both effects can be important for ILSE parameters and we believe that the lower limit on σ_o is more likely to restrict the maximum (linear) velocity tilt on the beam than is the upper limit of $\approx 85°$.

IV. Limits on Driver Magnet Aperture Ratios

Unless the lattice half-period L is reduced to 0.25 m or less, or the beam pipe opening is increased to 0.15 m or more, the magnetic transport section of ILSE should have more than an adequate safety margin in terms of particle loss or emittance growth. There remains the question, however, as too exactly how large the beam aperture ratio (a_b/L) may be in the magnetic transport section of a future HIF driver. This section of the paper first discusses some general properties of magnet lattices with large a_{wire}/L ratios and then presents simulation results for such magnets, both in terms of limits due to dynamic aperture and due to degradation of beam quality.

A. General Properties

Dr. Laslett's work on "Fourier-Bessel" magnets with azimuthally pure cos 2θ fields contains a general message: Periodic magnet lattices composed of full periods with identical winding patterns and whose current energizations are only slowly varying with cell number have magnetic fields which can be well-described by a general Fourier-Bessel mode decomposition. That is, if we presume that the windings are at a single radius a_{wire} and have four-fold azimuthal

symmetry, then we may generalize expression (20) for non-skew, surface current density to

$$\vec{J}(\theta, z) = \sum_{m=2,6,10,\ldots}^{\infty} \sum_{n=1,3,5,\ldots}^{\infty} \alpha_{m,n} \left[\cos\left(\frac{n\pi z}{L}\right) \cos(m\theta)\, \vec{e_z} + \frac{n\pi a_{wire}}{mL} \sin\left(\frac{n\pi z}{L}\right) \sin(m\theta)\, \vec{e_\theta} \right] \tag{22}$$

The corresponding magnetic scalar potential for $r < a_{wire}$ is then

$$\Phi_m(r, \theta, z) = -\frac{a_{wire}}{\mu_o} \sum_{m=2,6,10,\ldots}^{\infty} \frac{\sin m\theta}{m} \times \sum_{n=1,3,5,\ldots}^{\infty} \alpha_{m,n} \left(\frac{n\pi a_{wire}}{L}\right) K_m'\left(\frac{n\pi a_{wire}}{L}\right) I_m\left(\frac{n\pi r}{L}\right) \cos\left(\frac{n\pi z}{L}\right) \tag{23}$$

From the above expression, one can deduce a number of properties of the field topology scaling with a_{wire}:

1) If one desires to keep the field topography constant (*i.e.* at fixed locations) as a_{wire} is changed, then the product $a_{wire}^2 \alpha_{m,n} K_m'(n\pi a_{wire}/L)$ must be kept constant for each value of m and n. This implies that the relative strengths of the $\alpha_{m,n}$ and thus the current winding topography must change with a_{wire}. For $\zeta \ll 1$, $K_\nu'(\zeta) \propto \zeta^{-(\nu+1)}$. Hence, when $a_{wire} \leq L/2n$ (*i.e.* the magnet is long and skinny), $\alpha_{m,n}$ must scale as a_{wire}^{m-1}. On the other hand, when $\zeta > 1$, $K_\nu'(\nu\zeta) \propto \exp -(\nu\zeta)$. Consequently, the required surface current density for constant field topography must increase *exponentially* with the product (mna_{wire}) when $(a_{wire}/L) \geq n/m\pi$ (*i.e.* short, fat magnets).

2) If, conversely, one "freezes" the geometry of the current windings (*i.e.* by keeping constant the relative strengths of the $\alpha_{m,n}$ as would be true for a "three-term" magnet), the field topography will change as a_{wire} increases. To within 10% or less, the product of $K_\nu'(z)I_\nu(z) \approx -1/2z$ for all values of $z \geq 0$. Therefore, the value of $B_\theta \equiv (-1/r)\partial\Phi_m/\partial\theta$ at $r = a_{wire}$ is nearly independent of a_{wire} for a fixed values of the $\alpha_{m,n}$. For r, $a_{wire} \ll L/n\pi$ (*i.e.* a long, skinny magnet), the product of the two modified Bessel functions in Eq. (23) scales as (r^m/a_{wire}^{m+1}) and $B_\theta \propto r^{m-1}$, the same dependence as a 2-D azimuthal multipole of order m. When r, $a_{wire} \geq mL/n\pi$, the product of the Bessel functions is $\approx -\exp[-n\pi(a_{wire} - r)/L]/2\sqrt{a_{wire}r}$. In this case, B_θ increases exponentially with r with a scale length of

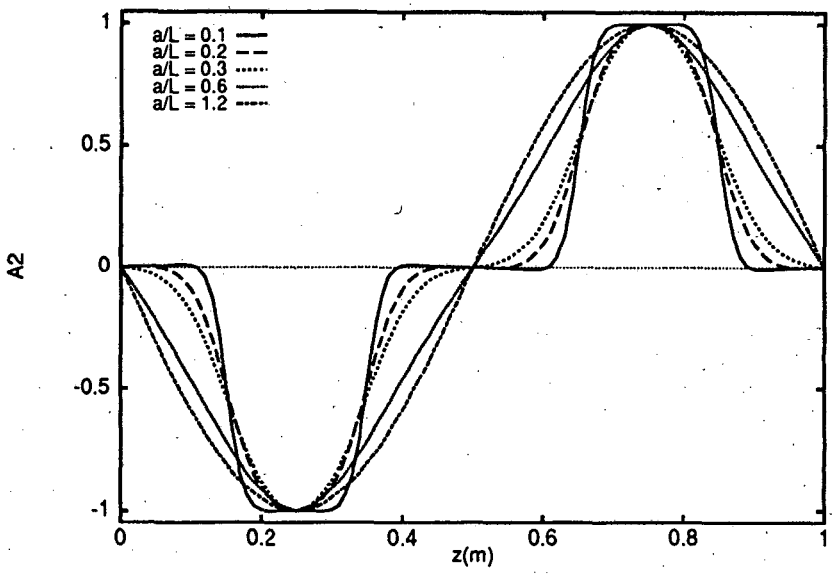

Figure 8: Magnitude of the midplane B_θ at $r = a_{wire}/2$ for an LBCF magnet with a_{wire} varying from $L/8$ to $L/2$.

$L/n\pi$. For a quadrupole magnet ($m = 2$), all non-zero longitudinal overtones (*i.e.* $n = 3, 5, 7, \ldots$) contribute strongly nonlinear focusing for particles traversing the outer half of the aperture when $a_{wire} \geq L/3$. When $r \ll L/n\pi$, the focusing will remain harmonic as before but with an exponentially damped magnitude relative to its value at a_{wire}. In the case of the dodecapole ($m = 6$) with $a_{wire} \approx L/3$, longitudinal overtones with $n \geq 7$ suffer similar exponential damping but the fundamental and first overtone will have close to the "2D" behavior of $B_\theta \propto r^5$.

Based on these observations, we make the following claim:

Beam transport in large aperture, quadrupolar magnetic focusing lattices with $a_{wire}/L > 1/3$ can be well-modeled by considering only the fundamental longitudinal Fourier component. If present, both higher order azimuthal modes and longitudinal overtones of the quadrupole will contribute strong nonlinear focusing for particles with $r \geq L/6$.

While it may be desirable to include higher longitudinal harmonics for ease of construction and/or for other reasons (*e.g.* diagnostic access), their contribution to the small amplitude tune will be quite small for large aperture quadrupole magnets. To illustrate this point, Fig. 8 contains plots of $A_2(z)$ for an LBCF magnet design with a_{wire}/L varying from 0.1 to 0.8. The particular design

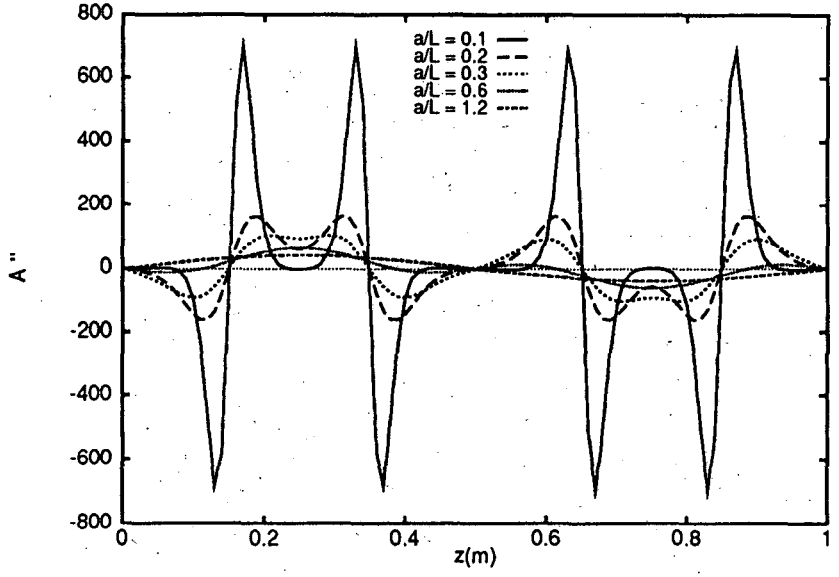

Figure 9: Strength of the mid-plane pseudo-octupole term versus z for various values of a_{wire}/L. Here, $A_2 a_{wire}^2$ has been normalized to the same peak value for each magnet.

had $L_k = 0.45\,L$ for all 12 wires [see Eq. (5)]. The curve for $a_{wire}/L = 0.1$ shows that A_2 is non-zero essentially only under the windings while the curve for $a_{wire}/L = 0.8$ is nearly a perfect sinusoid with period $2L$. Similar behavior is apparent in Fig. 9 for $A_2''(z)$, the pseudo-octupole. When $a_{wire}/L \ll 1$, $A_2''(z)$ is non-zero only near the beginning and end of the windings in each half-period. Because of the sharp change in the value of A_2 at the positions, $A_2''(z)$ has a large magnitude. As a_{wire}/L increases, A_2 "leaks" out from the magnet interior and $A_2''(z)$ drops sharply in magnitude (nearly as a_{wire}^{-2}). For $a_{wire}/L \geq 1$, fringe fields of adjacent half-periods begin to cancel each other, and A_2'', like $A_2(z)$, exhibits the asymptotic behavior of a simple sinusoid.

B. Dynamic Apertures with and without Space Charge

In earlier work, Laslett and Brady [9] examined the dynamic apertures of periodic, sinusoidally-varying quadrupole magnets (*i.e.* a one-term Fourier-Bessel lattice) as a function of the on-axis tune, σ_0. This study was limited to single particle motion and neglected space charge effects. They initialized "test" particles at discrete values of x and x' (with $y = y' = 0$) and then tracked their motion in phase space over hundreds of lattice periods. For $\sigma_0 = 72°$, they concluded that particles with $r \geq 0.4L$ would be lost. We confirmed this boundary using the HIFI code and found that the stability boundary at $\sigma_0 = 72°$ is associated with unstable fixed points with a corresponding phase advance is 90°. For the more general case of a completely emittance-dominated beam with an

initial KV distribution, the stability boundary is about $0.30L$ indicating that the stability boundary in r shrinks when x' and y' are non-zero.

The inclusion of space charge effects does not appear to change the stability boundary significantly. Test particles initialized with $x \leq 0.18$ m and $x' = y = y' = 0$ remained confined over 100 meters of transport for $L = 0.5$ m. However, beams with a matched $a_b \geq 0.20L$ and whose maximum envelope extent (including AG flutter) exceeded $0.30L$ suffered significant particle loss until the maximum envelope decreased to $0.26L$ or less. The exact type of initial phase space distribution (*e.g.* KV versus semi-Gaussian) did not seem to be of import.

To isolate the effects due to anharmonic focusing fields from those due to anharmonic space charge fields, we did another set of runs in which the space charge fields were determined from an envelope model (of constant emittance and uniform density). We tracked thousands of "test particles" that were initialized with a semi-Gaussian distribution with the same phase space moments as the envelope. Here too many particles whose r_{max} exceeded $0.30L$ became lost by the end of a 100-m simulation. Thus, we do not believe that the presence of anharmonic space charge terms critically affects the stability boundary. Exclusion of the $v_\perp \times B_z$ force term led to a more rapid particle loss with z but nearly the same asymptotic state as before in terms of total particle loss and final emittance.

From these results we conclude that the maximum "usable" dynamic aperture a_b of quadrupole magnet lattices whose fields are dominated by the fundamental Fourier-Bessel component is about $0.2L$ with the maximum permitted flutter somewhat below $0.3L$ for an undepressed tune of 72°. Beams of larger size will lose current, although there may be stable particle orbits whose maximum radii exceed this limit. Please note that "usable" refers to negligible particle loss, *NOT* to emittance growth which can be quite large at the large values of a_b/L.

A related question is the dependence of the maximum transportable line charge, λ_{max}, as a function of σ_o. Laslett and Brady [9] found in their single particle study that the maximum aperture increased by more than a factor of two when σ_o was reduced from 90° to 30°. However, since the focusing strength is proportional to the phase advance, it is not clear whether the maximum transportable current also increases, especially when collective space charge effects are included. A series of HIFI runs with constant λ, ε, but varying σ_o showed some intriguing results. As displayed in Fig. 10, the maximum aperture monotonically decreases with increasing σ_o while λ_{max} plateaus for relatively

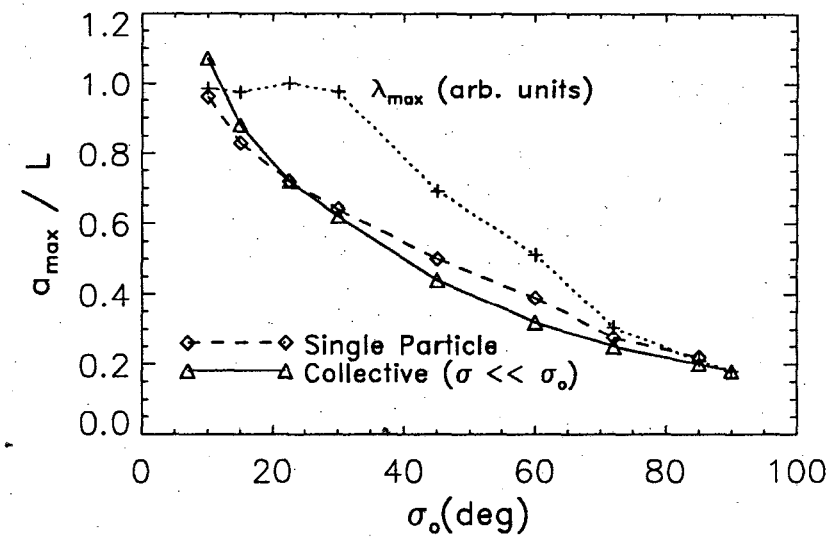

Figure 10: The maximum usable aperture a_{max} (*i.e.* that with negligible particle loss) normalized to half-period L and maximum transportable line charge λ_{max} (arbitrary units) plotted versus σ_o for a space-charge dominated beam. The dashed curve gives the equivalent maximum aperture when the beam is fully emittance dominated.

low values of σ_o but then falls off rapidly when σ_o exceeds 45°. This falloff appears to be due to resonant loss, *i.e.* particles encountering unstable fixed points in phase space and then being chaotically "spun off", although we did not investigate this point in any detail. As explained in the next section, the accuracy of the match at low σ_o became quite important and required use of nonlinear terms - inaccurate matches lead to excessive emittance growth and particle loss for the larger a_b/L ratios.

C. Emittance Growth in Large Aperture Quadrupole Lattices

Although large aperture magnets may be able to transport surprisingly large beams (in a physical sense) at low σ_o, there is generally large emittance growth when $a_b/L \geq 0.3$ caused by the beam edges encountering strongly nonlinear focusing fields. This subsection looks at the emittance growth issue and its dependence upon σ_o and (a_b/L). As in the previous section, we concentrate on periodic, sinusoidally-varying focusing fields (*e.g.* "Fourier-Bessel" magnets).

There are at least two related agents for emittance growth in large aperture magnetic quadrupoles. The first arises from phase-mixed damping of *macroscopic* mismatch oscillations. These became quite apparent first when running

HIFI simulations at low σ_o. Following useful discussions with and suggestions by I. Haber of NRL who had seen similar effects in the past [10],we modified HIFI's envelope matching algorithm (which predicts the proper values of $\bar{x}, \bar{x}', \bar{y}, \bar{y}'$ for use at $z = 0$) to use the total nonlinear field at the envelope boundary, rather than the harmonic, linear component only. This change forces a decrease in the matched radius, an effect most pronounced at low σ_o. For example, a HIFI run ($\lambda = 6.0\,\mu$C/m, 4 MV Ne^{+1}, $L = 0.5$ m, $\varepsilon_o = 900$ mm-mrad) with a linear match predicts that for $\sigma_o = 15°$, $a_{beam} = 446$ mm and 25% of the particles will be lost by 100 m. The equivalent run with the nonlinear matching algorithm predicts a matched radius of 283 mm and no charge loss over the same distance. The effects are smaller for $\sigma_o = 72°$, but still present. For $\lambda = 8.0\,\mu$C/m and $\varepsilon_o = 1200$ mm-mrad, a linear match predicts $a_b = 119$ mm and only $7.2\,\mu$C/m survives over 100 m of transport. The "correct" nonlinear match gives $a_b = 110$ mm and $7.5\,\mu$C/m survives over 100 m. From a small number of tests (with both the HIFI and SHIFTXY codes), it appears that using the value of the total nonlinear focusing at the $x-$ and $y-$ envelope boundaries as opposed to some area-weighted value (which would be smaller in magnitude) gives the best match properties.

A second type of emittance growth arises from a *microscopic* mismatch of the beam's initial 4D phase space distribution to the equilibrium distribution corresponding to the nonlinear focusing field (*i.e.* local force balance). If one includes both the pseudo-octupole term for the transverse magnetic field and the $v_\perp \times B_z$ terms when determining the AG-flutter-averaged focusing terms, one finds that

$$\sigma_o^2(r,\theta) = \sigma_o^2(0)\left(1 + \frac{3}{8}\left(\frac{\pi r}{L}\right)^2 - \frac{1}{8}\left(\frac{\pi r}{L}\right)^2 \cos 4\theta\right) \tag{24}$$

through terms second order in r/L. Here $\sigma_o(0)$ is the on-axis value of σ_o. This monotonic increase of σ_o with r causes $\rho(r)$ to evolve to a similar profile in order to reach force equilibrium between the space charge and external focusing. Likewise, the octupole term forces the development of an octupole moment in configuration space. If one neglects the external focusing B_z terms, the octupole term reverses in sign, an effect confirmed by HIFI simulations. The author cautions others that similar effects are possible in electrostatic simulations of FODO lattices if quadrupolar E_z terms are neglected at low energies.

By artificially including a z-independent octupole focusing term of the same size as predicted by expression (24), we could nearly eliminate the development of a spatial octupole moment in some low σ_o HIFI runs with $a_b/L \approx 0.5$ and a nonlinear match algorithm. However, the emittance growth in these runs, compared to those without the octupole focusing term, was reduced by only

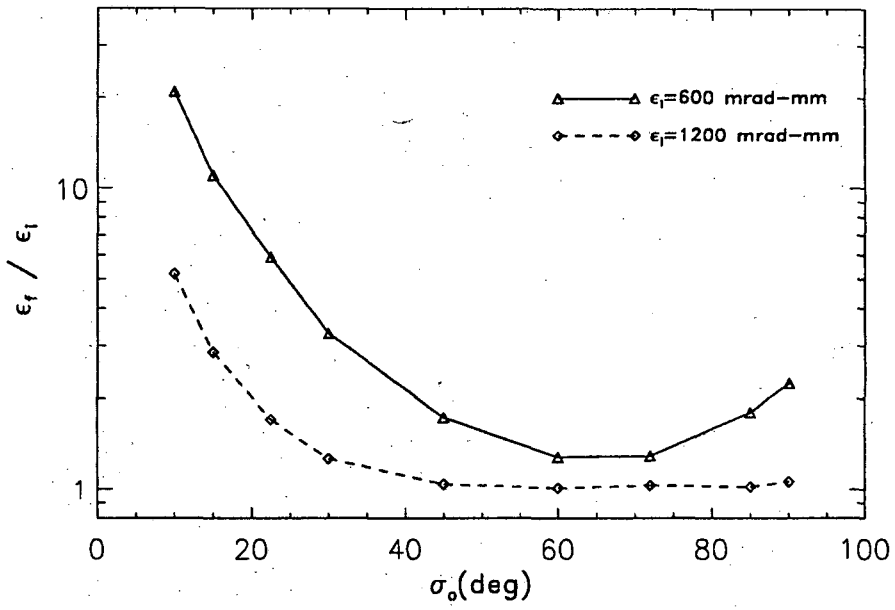

Figure 11: Emittance growth versus σ_o for 100-m of transport for an ILSE-like beam of 4μ C/m. At $\sigma_o = 72°$, $a_b/L \approx 0.15$ and $\sigma/\sigma_o \approx 0.1$ for $\varepsilon = 600$ mm-mrad and 0.3 for $\varepsilon = 2400$ mm-mrad. Particle loss occurs for $\sigma_o \geq 85°$, especially at the higher value of emittance.

about 15%. This indicates that the θ-independent term proportional to r^2 in Eq. (24) underlies the dominant mechanism for emittance growth.

The emittance growth resulting from microscopic profile and internal temperature changes in well-matched (*macroscopically*) beams is not necessarily small. In Fig. 11, we plot the ratio of $\varepsilon_f/\varepsilon_i$ as a function of σ_o for an ILSE-like beam of $4\,\mu$C/m in a 1-meter lattice for two values of initial emittance. The initial envelope parameters were determined by the nonlinear match algorithm; when $\sigma_o \geq 85°$, the beam radius begins to exceed the dynamic aperture of the lattice. From this curve, it is obvious that high current beams in low σ_o transport systems can have a great deal of emittance growth relative to those in high σ_o systems. This dependence suggests that if the final emittance is of concern (as it almost always is for HIF applications), it is better to transport moderate currents at a high σ_o rather than large currents at a low σ_o.

This tradeoff of large current, beam size, and emittance growth versus small current, beam size, and emittance growth is emphasized by Fig. 12 which plots $\varepsilon_f/\varepsilon_i$ versus a_b/L (and equivalently λ) for three values of σ_o. For these runs,

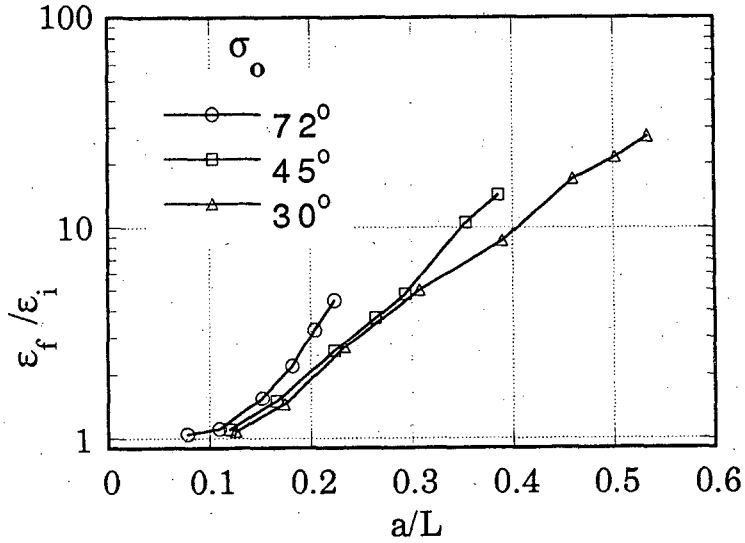

Figure 12: Emittance growth versus a_b/L over 100-m of transport for three values of σ_o for an ILSE-like beam. Each curve was terminated when particle losses exceeded a few per cent. For identical values of a_b/L, the transported λ is much larger at $\sigma_o = 72°$ than at $\sigma_o = 30°$.

we kept the beam brightness constant (*i.e.* $\varepsilon \propto \lambda^{1/2}$) with $\sigma \approx 6°$ at $1\,\mu$C/m for $\sigma_o = 72°$. For each choice of σ_o, the emittance more than doubles when a_b/L exceeds ≈ 0.2 and grows nearly 10-fold for $a_b/L \geq 0.4$, due to the rapid increase of strength of the nonlinear focusing terms at these larger radii.

A rough, analytical estimate of the emittance growth due to the nonlinear focusing terms of expression (24) may be obtained as follows: If we presume the final beam radius differs little from the initial beam radius (as would generally be true for a space-charge dominated beam), then the emittance increase is due nearly solely to the increase in $< v_\perp^2 >$. If the initial condition is a spatially uniform profile matched to the harmonic portion of $\sigma_o(r)$, then the nonlinear portion of (24) represents "excess" potential energy than can be converted to transverse emittance after extensive phase-mixed damping. Thus, for large z, we expect

$$\left\langle\left\langle \frac{m\Delta v_\perp^2}{2} \right\rangle\right\rangle \sim \left\langle\left\langle \int_{r_{i,n}}^{r_{f,n}} F_{NL}(r')\,dr' \right\rangle\right\rangle \tag{25}$$

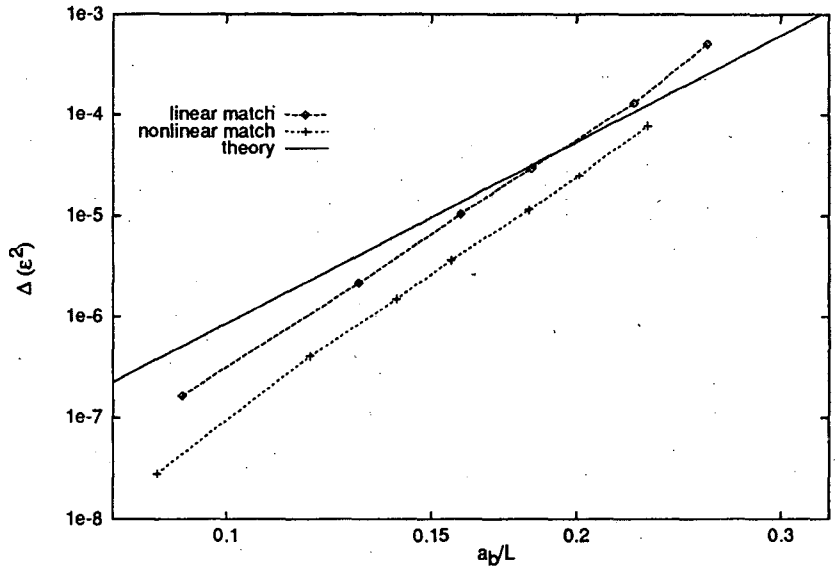

Figure 13: Growth in ε^2 versus initial a_b/L for both linear and nonlinear matches over 60-m of transport with $\sigma_o = 30°$. The solid line refers to the prediction of Eq. (26).

where the double bracket signifies an ensemble average over both the initial particle positions $r_{i,n}$ and final particle positions, $0 \leq r_{f,n} \leq r_{i,n}$. With these admittedly "ballpark" assumptions, we find

$$\Delta\left(\varepsilon^2\right) \approx \frac{5}{64}\left(\frac{\pi}{L}\right)^2 \left(\frac{\sigma_o}{2L}\right)^2 a_b^6 \tag{26}$$

where σ_o is measured in radians and $\Delta(\varepsilon^2)$ is the change in the edge emittance squared. In Fig. 13, we plot $\Delta(\varepsilon^2)$ versus a_b/L for a series of HIFI simulations with $\sigma_o = 30°$ together with the predictions of relation (26). For beams matched to the linear focusing terms, the simulations show a somewhat steeper dependence on a_b, perhaps due to higher order nonlinearities (*i.e.* $> r^4$) in the focusing potential becoming important. The figure also includes results from runs using the nonlinear match algorithm. These points are typically lower by a factor of 2-3 but also show a somewhat steeper dependence on a_b.

For better analytical predictions of emittance growth, one can apply the powerful methods of Lee [11] who showed

$$\frac{1}{v_z^2}\frac{d}{dz}\left\langle \frac{v_\perp^2}{2} \right\rangle = \int_0^\infty r\,dr\; k_{\beta,eff}^2 \frac{1}{I_b}\frac{\partial}{\partial z} I_{b,r} \tag{27}$$

where $k_{\beta,eff}$ is the effective radial focusing (*i.e.* external focusing - space charge defocusing) wavenumber and $I_{b,r}$ is the beam current contained within radius

r. For the simple case of both an initial and final flat beam profile with $a_{b,f} = (1-\delta)a_{b,i}$ and $\delta \ll 1$, the predicted change in edge emittance is

$$\Delta\left(\varepsilon^2\right) \approx \frac{\delta}{2}\left(\frac{\pi}{L}\right)^2\left(\frac{\sigma_o}{2L}\right)^2 a_b^6 \tag{28}$$

which has the same dependence upon a_b and L as did expression (26). More accurate results require knowledge of the final beam profile (which most certainly is not flat). Our work on this topic is at a rudimentary stage and will be reported on in the future if progress permits.

V. Conclusions

This memo has summarized our simulation results for space-charge dominated beam transport through various quadrupole magnet designs. For ILSE, we believe that there are a number of different designs that will transport the expected beam line charge of $1.0\,\mu$C/m of K^{+1} at 4.5-MV energy without any significant difficulties such as emittance growth or beam loss, so long as a reasonable clearance is maintained between the beam edge and inner pipe wall. Unless the half-period L is reduced to 0.3 m or less or the magnet wire radius a_{wire} increased to 0.15 m or greater, we do not predict any anomalous transport phenomena caused by fringe field nonlinearities. It will be important to match the ILSE beam properly from the 4:1 beam combiner to the magnetic transport lattice because focusing nonlinearities provide an efficient mechanism to thermalize electrostatic mismatch energy into emittance growth.

We have *not* examined the effects of iron yokes or winding errors, and the relative susceptibility of each magnet design to such, nor have we studied the effects of symmetry-breaking phenomena such as wire leads to the outside world. Magnet coil end designs similar to those proposed by Laslett, Caspi, and Helm have sufficiently large enough wire radii of curvature for $a_{wire} \geq 60$ mm that present-day superconducting cable can be employed, if desired, in these magnets.

Based upon Laslett's Fourier-Bessel decomposition of magnetic fields in periodic lattices, we believe that when a_{wire}/L exceeds 0.3 or so, the on-axis field becomes dominated by the fundamental longitudinal Fourier component $\propto \sin(\pi z/L)$. The magnet's effective length thus approaches the asymptotic value of $(2/\pi)L$ when normalized to the peak, on-axis field value at the center of each magnet. For $\sigma_o = 72°$, the maximum beam envelope size that can be transported without particle loss is $\approx 0.3L$ for both emittance- and space-charge dominated beams. The maximum current (and beam size) that can be transported through this type of magnet without loss is a strong function

of σ_o, with nearly three times greater current possible at $\sigma_o = 15°$ than at $\sigma_o = 72°$. On the other hand, it is extremely difficult to match large beams ($a_b/L \geq 0.5$) properly into the lattice because the bulk of the beam encounters highly nonlinear focusing fields. Moreover, even if the beam is well matched in a macroscopic sense, the emittance will grow as the microscopic beam profile and internal temperature adjust to the nonlinear fields. In general, these matching difficulties will lead to significant emittance growth and it appears best to keep σ_o in the range of 60° to 80° and $a_b/L \leq 0.15 - 0.2$ when transporting HIF beams. This also will minimize peak magnetic fields (since as a_{wire}/L increases beyond 0.25, B begins to increase exponentially). However, if one is concerned only with peak current and not emittance, as might be true for accelerators used for material irradiation or neutron production, the low σ_o systems might be of interest.

Appendix A: Determining $\vec{B}$ via Magnetic Scalar Potential

If one neglects the current leads to and from an air core electromagnet, Ampere's law inside the windings becomes

$$\nabla \times \vec{B} = \frac{4\pi}{c}\vec{J} = 0 \quad \text{and thus} \quad \vec{B} = -\nabla\Phi_m \tag{29}$$

where Φ_m may be identified as the magnetic scalar potential. To determine Φ_m for a particular current loop with circulating current I, we note that

$$B_i = -\hat{i}\cdot\nabla\Phi_m = \frac{I}{c}\hat{i}\cdot\oint\frac{d\vec{l}\times\vec{r}}{r^3} = \frac{I}{c}\oint d\vec{l}\cdot\frac{\left(\vec{r}\times\hat{i}\right)}{r^3} \tag{30}$$

where $\hat{i}$ is a Cartesian unit vector, $d\vec{l}$ is an infinitesimal segment of the current loop, and $\vec{r}$ is the radial vector directed from the segment to the observer position.

Applying Stoke's Theorem to the rightmost integral results in

$$-\hat{i}\cdot\nabla\Phi_m = \int\left(\nabla\times\frac{\vec{r}\times\hat{i}}{r^3}\right)\cdot d\vec{A} = \int\hat{i}\cdot\nabla\left(\frac{\vec{r}\cdot d\vec{A}}{r^3}\right) \tag{31}$$

Hence,

$$\Phi_m \equiv -\frac{I}{c}\int\frac{\vec{r}\cdot d\vec{A}}{r^3} \tag{32}$$

and the magnetic scalar potential is proportional to the projected solid angle occupied by the given current loop.

While the magnetic scalar potential Φ_m does not contain any additional information than does the more familiar magnetic vector potential $\vec{A}$, its "conciseness" may be advantageous in that it is only necessary to specify one value at a given position as opposed to three. This may prove useful for applying the Differential Algebra (DA) numerical methods, currently under study by S. Caspi, L.J. Laslett, and M. Helm in connection with magnetic field determinations.

All of the magnets studied in this note have the useful property that individual wire turns lie on cylinders of constant radius. Despite the resultant current loop having a curved surface, one can exploit this fact and make significant progress in calculating Φ_m, and, more importantly, B_θ.

Denoting the observer's position in cylindrical coordinates as (ρ, θ, z) and the surface element $d\vec{A}'$ as $\rho'\, d\vec{\theta}' \times d\hat{z}'$, we find

$$\left(\vec{r}' - \vec{r}_{obs}\right) \cdot d\vec{A}' = \left[\rho' - \rho\cos\left(\theta' - \theta\right)\right] \rho'\, d\theta'\, dz' \tag{33}$$

and

$$\Phi_m\left(\rho, \theta, z\right) = -\frac{I}{c} \int_{\theta_1'}^{\theta_2'} \rho'\, d\theta' \int_{z_1(\theta')}^{z_2(\theta')} \frac{\left[\rho' - \rho\cos\left(\theta' - \theta\right)\right] dz'}{\left(\alpha^2 + \left(z' - z\right)^2\right)^{3/2}} \tag{34}$$

where $\alpha^2 \equiv \rho'^2 + \rho^2 - 2\rho\rho'\cos\left(\theta - \theta'\right)$ and $z_1(\theta'), z_2(\theta')$ describe the longitudinal extent of the current loop at position θ'.

The integral over z' is straight-forward giving

$$\Phi_m\left(\rho, \theta, z\right) = -\frac{I}{c} \int_{\theta_1'}^{\theta_2'} \rho'\, d\theta' \left.\frac{\left[\rho' - \rho\cos\left(\theta' - \theta\right)\right]\left(z' - z\right)}{\alpha^2\left(\alpha^2 + \left(z' - z\right)^2\right)^{1/2}}\right|_{z' = z_1'(\theta')}^{z' = z_2'(\theta')} \tag{35}$$

At this point, there seems to be no obvious way to progress further in the general problem. However, *if* $z_1'(\theta'), z_2'(\theta')$ are *not* functions of θ', one can exploit the fact that θ and θ' appear in Eq. (35) only in the argument of $(\theta' - \theta)$ rather than individually. Hence it follows that

$$\begin{aligned} B_\theta\left(\rho, \theta, z\right) &= -\frac{1}{\rho}\frac{\partial}{\partial\theta}\Phi_m \\ &= -\frac{I}{c}\left[\frac{a - \rho\cos\left(\theta - \theta'\right)}{\alpha^2}\left\{\frac{z' - z}{\left(\alpha^2 + \left(z' - z\right)^2\right)^{\frac{1}{2}}}\right\}\Bigg|_{z_1'}^{z_2'}\right]\Bigg|_{\theta_1'}^{\theta_2'} \end{aligned} \tag{36}$$

This result can also be obtained directly from the more conventional Biot-Savart algorithm.

To deal with the more general case of a curved $z(\theta)$ end, we can obtain a good numerical approximation by subdividing the region in θ' in a "staircase" fashion and add up the individual "stair" contributions to B_θ. This is the approach taken by the XSQUAD code to deal with curved boundaries. To maintain reasonably high accuracy, the staircase width in θ' is kept ≈ 0.02 radians or less.

Appendix B: HIFI Simulation Code

HIFI† is a particle simulation code recently developed by the author to study transport phenomena in periodic, strong-focusing lattices. The original emphasis was speedy computation and HIFI first used a simple, gridless field solver and the paraxial approximation. However, as the focus shifted to accurate emittance growth determination for beams in highly nonlinear fields, more complicated field solvers and particle pusher algorithms were used. Still, a typical HIFI run with 4096 particles and 6000 z-steps takes only ≈2-3 minutes of CRAY-1 equivalent CPU time. Some important features of the current version of the code include:

Macroparticle beam representation
As is true for most particle simulation codes, HIFI uses a limited number (1024-8192) "macroparticles" to represent the 4-D distribution of $\geq 10^{10}$ true ions in a transverse beam slice. The beam is initialized with either a KV or semi-Gaussian distribution with a bit-reversed quiet start used to scramble both $\theta_{x,y} = \tan^{-1} x_i/y_i$ and $\theta_v = \tan^{-1} v_{x,i}/v_{y,i}$. For semi-Gaussian loads, one additional bit-reversal is done for the absolute magnitude of the initial particle transverse velocity.

We matched the beam at the midpoint of a quadrupole (where $\overline{x^2}' = \overline{y^2}' = 0$) via an empirical procedure suggested by I. Haber, and then integrated the equations of motions backwards to the middle of a drift section (the "O" in the FODO lattice) to get the "true" start conditions for the simulation. At present, the code presumes even symmetry in both the x- and y-planes centered around the instantaneous beam centroid for purposes of space charge collection and transverse electric field solution. This assumption strongly reduces the number of particles and azimuthal field nodes needed. In future HIFI versions, we plan to relax this assumption.

† So named for an obscure Japanese goddess of consumer electronics, little known to occidental tourists or pundits.

Particle Pusher
HIFI follows x, y, v_x, and v_y for each particle employing a leapfrog scheme with z rather than t as the independent variable. When the paraxial approximation is used, v_z is presumed constant and equal for all particles in the transverse slice with

$$v_{z,0} \equiv \left(\frac{2eV}{m}\right)^{1/2} \tag{37}$$

i.e. v_x and v_y are presumed to be vanishingly small relative to v_z. For the simulation results presented in this paper, the particle voltage V is constant with z.

For cases where $a_b/L \geq 0.15$, v_x/v_z can exceed 0.2 or greater and the paraxial approximation is of questionable accuracy. HIFI treats non-paraxial motion in the following way. Let us adopt the convention that in HIFI's leapfrog scheme, the velocities are known on the half-step and the particle positions and fields on the integer steps. Then the general force equation

$$\frac{d\vec{v}}{dt} = \frac{e\vec{E}}{m} + \frac{e\vec{v}}{mc} \times \vec{B} \tag{38}$$

can be approximated by

$$\frac{\vec{v}_{\perp,n+1/2} - \vec{v}_{\perp,n-1/2}}{\Delta z} \equiv \frac{e\vec{E}_{\perp,n}}{mv_{z,0}} + \left(\frac{\vec{v}_{z,n}}{\vec{v}_{z,n}}\right) \frac{\hat{z} \times e\vec{B}_{\perp,n}}{mc} + \frac{\vec{v}_{\perp,n}}{v_{z,n}} \times \frac{e\vec{B}_{z,n}}{mc} \tag{39}$$

Here $\vec{v}_{\perp,n}$ is determined as in the classic "Boris" mover (see *e.g.* Birdsall and Langdon [12]) and

$$v_{z,n} \equiv \left[v_{z,0}^2 - v_{x,n}^2 - v_{y,n}^2\right]^{1/2} \tag{40}$$

There is an obvious inconsistency with the above algorithms in that the electric field acceleration changes the particle energy which invalidates expression (40). Furthermore, the denominator of the first term of the RHS of (39) should be $v_{z,n}$, not $v_{z,0}$. We used $v_{z,0}$ because the present acceleration algorithm collects the sum of $\vec{E}_\perp + \vec{v}_{z,0} \times \vec{B}_\perp/c$ rather than the electric and magnetic acceleration components separately. The fractional error is $\approx (v_\perp^2/2v_z^2)$ which is typically a few percent or less. In the near future, we will modify HIFI to avoid this problem by collecting E and B separately and, moreover, advance v_z from a force equation rather than an inexact conservation-of-energy equation. The position advance for x is

$$\frac{x_{n+1} - x_n}{\Delta z} = \frac{v_{x,n+1/2}}{v_{z,n+1/2}} \tag{41}$$

with $v_{z,n+1/2}$ given from the equivalent of expression (40).

Field Solver
The early versions of HIFI employed a simple field solver in which the beam profile was presumed to be that of an uniformly-filled ellipse, irrespective of the actual distribution. The major and minor semi-axes were defined to be

$$\bar{a} \equiv 2\,\max(x_{rms}, y_{rms}) \quad \text{and} \quad \bar{b} \equiv 2\,\min(x_{rms}, y_{rms}) \tag{42}$$

The resultant electrostatic potential is then harmonic and simply determined. The field exterior to the ellipse was then analytically determined using Laslett's formulation [13] in elliptic coordinates or, optionally, simply presumed to follow the same harmonic dependence as the interior.

While this field solver is extremely fast and simple, it is also extremely inaccurate for beams suffering significant distortion from nonlinear focusing terms. After a number of months exploring various alternative field solvers (*e.g.* self-similar elliptical shells in elliptic coordinates, gridless cylindrical multipole decompositions), we settled on a fairly standard method of 2D (r, θ) gridded, multipole decomposition. At present the outer boundary is "open" and there are no forces due to image charge on a conducting beam pipe.

The radial grid was chosen to be uniform in r^2. While this choice decreases resolution near the axis, it should minimize growth caused by statistical fluctuations of particle number. With a purely electrostatic field solver, the grid could "breathe" in and out with the beam's semi-major axis, with of order 16-24 radial grid zones enclosing the full beam. A small number of tests indicated the use of this type of dynamic grid appeared to have negligible effect upon numerical emittance growth. Rather, the magnitude of the AG flutter motion and the number of macroparticles play a much greater role. The azimuthal grid was uniform, with generally 16 zones per quadrant and azimuthal modes through $\cos 16\theta$ determined.

The magnetic field strength at each particle's position was calculated analytically, using an expansion equivalent to (2). For magnets where $A_2(z)$ was computed numerically on an uniform z-grid, B_z was found from the numerical value of $A_2'(z)$; this was not necessary for Bessel-Fourier magnets where an analytic expression for B_z exists.

Diagnostics
HIFI computes RMS emittance in both the x- and y-planes using the standard Lee-Cooper algorithm [14]). The "edge" emittance is defined to be $4\varepsilon_{rms}$ as is true for a KV distribution. As is well known, in situations where there is a

beam "halo" in transverse phase space, the magnitude of ε_{rms} is sensitive to the exact cutoff employed (*e.g.* including all particles out to r_{pipe} versus the interior, cumulative 95% population). We chose $r_{cutoff} \equiv \min(r_{pipe}, 3a_{1/2})$ where $a_{1/2}$ is the radius that contains one-half of the beam particles.

HIFI also follows two sets of "test particles" for particle tracking purposes. These particles do not contribute to the beam's charge when computing the electric field. One set is initialized with betatron orbits of differing $x - y$ eccentricities and maximum amplitude. History plots of $x - y$ positions made at the end of the simulation run show both the high frequency A-G flutter and the low frequency betatron motion. Another set of test particles can be initialized on the $\mathbf{x} - \mathbf{x}'$ or $\mathbf{y} - \mathbf{y}'$ plane with point history plots of their phase space positions at homologous z-positions (relative to the lattice period $2L$) showing regions of stable and unstable fixed points. Such plots are extremely useful in determining aperture stability boundaries.

At user-specified z–positions, scatter plots are made of $x - y$, $x - v_x$, *etc.* particle positions in phase space. These are useful in showing obvious beam distortions such as halo formation. In addition, the SUN workstation version of HIFI can run in "movie-mode" where a $x - y$, $x - x'$, or $r - v_r$ scatter plot is continually updated on the screen. This feature proved useful in picking up the dodecapole-AG flutter resonance possible in LCH magnets. It also showed that the development of "butterflies" in phase space follows from the radial variation of σ_o.

References

1. L.J. Laslett, *Fields of a Provisional Downstream Magnetic Quadrupole for ILSE*, HIFAR-167,168 (1987).

2. P. Krejcik, *Conference Record of the 1987 IEEE Particle Accelerator Conference*, 2, 1278 (1987).

3. F.E. Mills and G.H. Morgan, Part. Accel. 5, 227 (1973).

4. L.J. Laslett, S. Caspi, M. Helm, Part. Accel. 22, 1 (1987).

5. V. Brady, *2-D Dipole Windings*, HIFAR-145 (1987);

   V. Brady, *12 Wire 3-D Dipole*, HIFAR-147 (1987).

6. I. Hofmann, L.J. Laslett, L. Smith, and I. Haber, Part. Accel. 13, 145 (1983).

7. M.G. Tiefenback, *Space-Charge Limits on the Transport of Ion Beams in a Long Alternating Gradient System*, LBL-22465 (1986).

8. M.G. Tiefenback and D. Keefe, *Proc. 1985 Part. Accel. Conf.*, IEEE Trans. Nucl. Sci. NS-32, 2483 (1985).

9. L.J. Laslett, *Aperture Ratio and Related Transport Limitations*, HIFAN-427 (1989).

10. I. Haber and H. Rudd, Nucl. Inst. Meth, Phys. Res. A278, 174 (1989).

11. E.P. Lee, *Determination of the Radius of a Self-Pinched Beam from Its Energy Integral*, LLNL UCID-18495 (1980).

12. C.K. Birdsall and A.B. Langdon, *Plasma Simulation via Particle Simulation*, McGraw-Hill, New York, pp. 59-60 (1985).

13. L.J. Laslett, ERAN-44 (1969), reprinted in LBL PUB-616, Vol. III, 113 (1987).

14. E.P. Lee and R.K. Cooper, Part. Accel. 7, 81 (1976).

LAWRENCE BERKELEY LABORATORY
UNIVERSITY OF CALIFORNIA
TECHNICAL INFORMATION DEPARTMENT
BERKELEY, CALIFORNIA 94720